PRINTABLE SOLID-STATE RECHARGEABLE POWER SOURCES VIA HETERO-COLLOIDAL CHEMISTRY CONTROL

Se-Hee Kim

Department of Energy Engineering

(Battery Science and Technology)

Graduate School of UNIST

2019

PRINTABLE SOLID-STATE RECHARGEABLE POWER SOURCES VIA HETERO-COLLOIDAL CHEMISTRY CONTROL

Se-Hee Kim

Department of Energy Engineering
(Battery Science and Technology)

Graduate School of UNIST

Printable Solid-State Rechargeable Power Sources *via* Hetero-Colloidal Chemistry Control

A thesis/dissertation
submitted to the Graduate School of UNIST
in partial fulfillment of the
requirements for the degree of
Doctor of Philosophy of Science

Se-Hee Kim

12. 10. 2018

Approved by

Advisor

Sang-Young Lee

Printable Solid-State Rechargeable Power Sources *via* Hetero-Colloidal Chemistry Control

Se-Hee Kim

This certifies that the thesis/dissertation of Se-Hee Kim is approved.

12. 10. 2018 of submission

Advisor: Sang-Young Lee

Kwanyong Seo

Jae Sung Son

Jang-Ung Park

Chang-Hyeon Kim

Abstract

Forthcoming smart energy era, which will find widespread use of flexible/wearable electronic devices, Internet-of-Things (IOTs), electric vehicles (EVs) and grid-scale energy storage systems (ESSs), is in relentless pursuit of high-energy/safe rechargeable power sources. The rechargeable energy storage systems could be suggested as a promising solution to fulfill the stringent requirements for flexible electronics. From the cell manufacturing point of view, conventional rechargeable batteries with fixed shapes and sizes are generally fabricated by winding (or stacking) cell components (such as anodes, cathodes and microporous separator membranes) and then packaging them with (cylindrical-/rectangular-shaped) metallic canisters or pouch films, finally followed by injection of liquid electrolytes. In particular, the use of liquid electrolytes gives rise to serious concerns in cell assembly because they require strict packaging materials to avoid leakage problems and also separator membranes to prevent electrical contact between electrodes. For these reasons, the conventional cell assembly and materials have pushed the batteries to lack of variety in form factors, thus imposing formidable challenges on their integration into versatile-shaped electronic devices.

Printing is known to be a simple and reliable technique capable of imparting various surface functionality to a wide diversity of substrates. Recently, besides traditional application fields of printing technology for commodity interests, printed electronics has emerged as an attractive industry due to its process benefits enabling facile fabrication of solution-processable thin-film transistors and integrated circuits.

In this dissertation, focused on development of printable solid-state rechargeable power sources (including lithium-ion and lithium-sulfur batteries) with exceptional form factors and aesthetic versatility, which lie far beyond those achievable with conventional battery technologies. In addition, rheo-electrical properties of the printable battery components are systematically elucidated to better understand bi-continuous ion/electron transport phenomena and also printing processability.

Contents

List of figures

(b) Rheological properties of printable LFP cathode slurry (LFP/carbon black additive/SCE matrix precursor = 38/4/58 (w/w/w) without NMP solvent).

Figure 14. Rheological properties of printable LTO anode slurry (LTO/carbon black additive/SCE matrix precursor = 27/7/66 (w/w/w) without NMP solvent) for a PRISS cell: (a) viscosity; (b) storage modulus (G') and loss modulus (G").

Figure 15. Effect of solid content (= LFP powders + carbon black) in printable LFP cathode slurries on rheological properties. At lower solid content (= 20 wt.%): (a) viscosity; (b) storage modulus (G') and loss modulus (G"). At higher solid content (= 50 wt.%): (c) a photograph showing the poor dispersion state (*i.e.*, serious agglomeration of particles) in the cathode slurry.

Figure 16. Morphological characterization (cross-sectional view) of printable electrodes, LFP cathode: (a) SEM images; (b) EDS images, LTO anode: (c) SEM images; (d) EDS images.

Figure 17. Change in the FT-IR spectra of acrylic C=C double bonds of ETPTA before/after UV irradiation: (a) printable LFP cathode; (b) printable LTO anode.

Figure 18. (a) Photographs showing mechanical flexibility of printable electrodes upon physical deformation such as folding and winding (rod diameter = 5 mm). (b) Photographs of the letters-shaped LFP cathode slurry (represented by a word of "UNIST", upper image)

Figure 19. A schematic illustration of the UV-IL technique-driven micropatterning procedure and a SEM photograph showing the printable LFP cathode with inverse replica of the finely-defined microscale stripe pattern.

Figure 20. Major characteristics of printable SCE layers: (a) viscosity; (b) G' and G"; (c) microscale imprintability; (d) mechanical flexibility; (e) temperature-dependent ionic conductivity.

Figure 21. Galvanostatic charge/discharge profiles of (a) LFP half cell (= printable LFP cathode (LFP/carbon black/SCE matrix = 38/4/58 w/w/w)/(1M $LiPF_6$ in EC/PC)-soaked PE separator/lithium metal anode) as a function of cycle number, wherein the PE separator was previously treated by 1N H_2SO_4 solution to facilitate the uptake the EC/PC-based liquid electrolyte. The cell was cycled at a fixed charge/discharge current density of 0.1 C/0.1 C under a voltage range of 2.5 - 3.8 V, where the gravimetric charge/discharge capacity was estimated

based on the mass of LFP active materials, (b) LTO half cell (= printable LTO anode (LTO/carbon black/SCE matrix = 27/7/66 w/w/w)/(1M $LiPF_6$ in EC/PC)-soaked PE separator/lithium metal anode) as a function of cycle number, where the PE separator was previously treated by 1N H_2SO_4 solution to facilitate the uptake EC/PC-based liquid electrolyte. The cell was cycled at a fixed charge/discharge current density of 0.1 C/0.1 C under a voltage range of 1.0 - 2.5 V, where the gravimetric charge/discharge capacity was estimated based on the mass of LTO active materials.

Figure 22. (a) A SEM image (cross-sectional view) of a PRISS full cell (= printable LFP cathode (LFP/carbon black/SCE matrix = 38/4/58 w/w/w)/printable SCE layer (ETPTA/1M $LiPF_6$ in EC/PC/Al_2O_3 nanoparticles = 5/28/67 w/w/w)/printable LTO anode (LTO/carbon black/SCE matrix = 27/7/66 w/w/w)), wherein the EC/PC-based liquid electrolyte was removed prior to the SEM analysis. (b) Galvanostatic charge/discharge profiles of a PRISS full cell as a function of cycle number. The cell was cycled between 1.0 and 2.5 V at a constant charge/discharge current density (= 0.05 C/0.05 C), where gravimetric charge/discharge capacity was estimated based on the mass of LFP active materials. (c) SEM images (cross-sectional view) of the printable electrodes after the cycling test (30 cycles).

Figure 23. Conceptual comparison of cell design and shape (left image = conventional cell, right image = PRISS cell that can be shape-conformable and also seamlessly integrated with electronic devices).

Figure 24. A photograph showing direct fabrication of a PRISS cell on paper-made eyeglasses. The PRISS cell-unitized wearable eyeglasses operated a LED lamp.

Figure 25. A photograph showing direct fabrication of a heart-shaped PRISS cell on a transparent glass cup with curvilinear surface. The PRISS cell, under being mounted on the round-shaped glass cup, delivered normal charge/discharge behavior (at charge/discharge current density of 0.05 C/0.05 C under voltage range of 1.0 - 2.5 V, gravimetric charge/discharge capacity was estimated based on the mass of LFP active materials).

Figure 26. A photograph of "PRISS" letters-shaped PRISS cell (left side) and its charge/discharge profiles at charge/discharge current density of 0.05 C/0.05 C under voltage range of 1.0 - 2.5 V (right side, gravimetric charge/discharge capacity was estimated based on the mass of LFP active materials), which were measured under being completely wound along the rods having different diameters (= 5, 10, 15 mm), not a planar configuration.

Figure 27. Schematic illustration of the flexible/shape-versatile bipolar cells prepared via the UV-assisted multistage printing process.

Figure 28. Schematic of the procedure used to fabricate the stencil-printed GCE, along with photographs of the GCE and chemical structure of its major components. The GCE consisted of the gel electrolyte ((1 M $LiBF_4$ in SBN) electrolyte and semi-IPN skeleton) and Al_2O_3 nanoparticles.

Figure 29. Rheological properties and ionic conductivity of the GCE pastes as a function of the ratio of gel electrolyte/Al_2O_3 nanoparticles. (a) Shear rate-dependent viscosity and photographs (inset images). The GCE paste (gel electrolyte/Al_2O_3 = 20/80) failed to measure its rheological properties due to serious particle agglomeration. (b) Viscoelastic properties (G' and G'') of the GCE pastes as a function of shear stress. (c) Ionic conductivity of the printed GCE films as a function of temperature.

Figure 30. (a) Cross-sectional SEM and EDS images showing the dispersion state of Al_2O_3 nanoparticles and the presence of interstitial voids (originally occupied by the SBN-based electrolyte) in the printed GCE. (b) EDS mapping area of Al and F elements in the printed GCE.

Figure 31. Mechanical properties of GCE, (a) DSC thermograms showing two different T_{gs} of the ETPTA polymer network and PVdF-HFP in the semi-IPN. The insets show the (T_{gs}) of the pristine ETPTA polymer network and PVdF-HFP, respectively, (b) SEM morphology of the (ETPTA/PVdF-HFP = 75/25 (w/w)) semi-IPN film; the PVdF-HFP was selectively etched prior to the SEM analysis, (c) Change in the characteristic FT-IR peaks assigned to the acrylic C=C bonds (1610–1625 cm^{-1}) of the ETPTA in the printed GCE before/after UV irradiation, (d) The mechanical flexibility of the printed GCE upon the bending cycles (bending radius = 5 mm, deformation rate = 10 mm min^{-1}).

Figure 32. (a) The ionic conductivity of the printed GCE as a function of temperature. (b) TGA profiles of the GCE and carbonate-based control electrolyte (1 M $LiPF_6$ in EC/DMC = 1/1 (v/v)) chosen as the control electrolyte. (c) The isothermal (80 °C) ionic conductivity of the GCE and carbonate-based control electrolyte as a function of time. (d) The nonflammability test of the GCE (top photographs) and the carbonate-based control electrolyte (bottom photographs).

Figure 33. Schematic of the procedure used to fabricate the stencil-printed electrode, along with photographs of the electrode. The printed electrodes consisted of the gel electrolyte ((1 M $LiBF_4$

in SBN) electrolyte and semi-IPN skeleton), carbon black additive and an electrode active material (LCO and LTO powders were chosen for proof of concept).

Figure 34. Change in the characteristic FT-IR peaks assigned to the acrylic C=C bonds (1610–1625 cm^{-1}) of the ETPTA before/after UV irradiation: (a) printed LCO cathode and (b) printed LTO anode.

Figure 35. Cross-sectional SEM and EDS images showing the dispersion state of the LCO powders and the presence of interstitial voids (originally occupied by the SBN-based electrolyte) in the printed LCO cathode. (c) SEM image of the SWCNT-coated LCO powders. The inset shows the morphology of the pristine LCO powders.

Figure 36. (a) SEM image of the SWCNT-coated LCO powders. The inset shows the morphology of the pristine LCO powders. TGA profiles of the SWCNT-coated electrode active powders, (b) SWCNT-coated LCO, (c) SWCNT-coated LTO. Comparison of the electronic conductivity, (d) SWCNT-coated LCO and pristine LCO, (e) SWCNT-coated LTO and pristine LTO. (f) Comparison of the discharge rate capability between the SWCNT-coated LCO and pristine LCO, where coin-type half cells (Li metal anode/PE separator/LCO cathode) were examined at a constant charge current density of 0.1C.

Figure 37. (a) Change in the electronic resistance of the printed LCO cathode (vs. control LCO cathode (LCO/carbon black/PVdF binder = 95/2/3 (w/w/w)) prepared by slurry casting) as a function of the longitudinal compression cycle (bending radius = 5mm, deformation rate = 10mm min^{-1}). (b) Photographs showing the multi-folding of the printed LCO and control LCO cathodes.

Figure 38. Comparison of the thermal stability of the printed LCO and control LCO cathodes incorporating the carbonate-based liquid electrolyte (1 M $LiPF_6$ in EC/DMC = 1/1 (v/v)): (a) TGA profiles; (b) DSC thermograms showing interfacial exothermic reactions between delithiated LCO and electrolytes; (c) nonflammability tests of the printed LCO cathode (left photograph) and the control LCO cathode (right photograph).

Figure 39. (a) Viscosities of the GCE and electrode pastes as a function of shear rate. (b) Viscoelastic properties (G' and G'') as a function of shear stress. (c) Hysteresis loops in the rheograms. (d) Photographs showing the fabrication of the (letter-shaped) printed GCE (top photographs) and LCO cathode (bottom photographs) on miniature toy cars with curvilinear surfaces.

Figure 40. (a) Cross-sectional SEM image of the printed bipolar cells (here, the three cells were connected in series) and schematic of their structures, wherein the LTO anode and LCO cathode shared the Al foil as a common current collector. (f) Cross-sectional SEM image of the printed bipolar cells (here, the three cells were connected in parallel) and schematic of their structures.

Figure 41. (a) Charge–discharge profiles of the printed LCO cathode and LTO anode, where a coin-type half cell (printed LCO cathode (or printed LTO anode)/(1 M $LiBF_4$ in SBN)-soaked PE separator/lithium metal) was cycled at a fixed charge/discharge current density of 0.1C/0.1C in the voltage range from 3.0 to 4.2 V and from 1.0 to 2.5 V, respectively. (b) Cycling performance of the printed mono full cell (LCO cathode/GCE/LTO anode), where the cell was cycled between 1.5 and 2.7 V at a constant charge/discharge current density (0.05C/0.05C). Cross-sectional SEM image of the printed mono full cell (composed of an LTO anode, GCE layer and LCO cathode). (a) Before the cycle test. (b) After the 50^{th} cycle.

Figure 42. (a) The charge/discharge profiles of the printed bipolar cells connected in series as a function of cell number (1 - 3 cells). (b) Charge/discharge profiles at 1^{st}, 25^{th} and 50^{th} cycles. (c) Capacity retention as function of cycle number. (d) Comparison of the charge/discharge profiles of the printed bipolar cells (in-series vs. in-plane).

Figure 43. Mechanical flexibility and thermal stability of the printed bipolar cells. (a) Charge/discharge profiles of the printed bipolar 2-stacked cell (*i.e.*, the two cells were connected in series) before/after 100 bending cycles (bending radius = 20 mm, deformation rate = 200 mm min^{-1}). (b) Photographs showing the safety robustness of the printed bipolar 2-stacked cell. The cell continued to power an LED lamp even after being horizontally cut in half. (c) Charge/discharge profiles of the printed bipolar 2-stacked cell before/after exposure to thermal shock (130 ^{o}C/0.5 h). The photograph of the cell after the thermal shock test, along with that of the control cell (consisting of LCO cathode, LTO anode, carbonate-based electrolyte (1 M $LiPF_6$ in EC/DMC = 1/1 (v/v)) and PE separator) is also shown. (d) Photographs showing the stepwise fabrication of the printed bipolar 2-stacked cell on the curved roof of a miniature toy car. (e) Charge/discharge profiles of the printed bipolar 2-stacked cell on a miniature toy car. (f) Nonflammability test of the printed bipolar 2-stacked cell and control cell; the Al pouch-based packaging substances were removed prior to this test.

List of tables

CHAPTER I. Introduction

1.1 Introduction of Lithium based Rechargeable Power Sources

1.1.1 Overview of Lithium-Ion Batteries

Lithium-ion batteries (LIBs) are common rechargeable batteries for portable electronics, with a high energy density, high voltage window, long cyclability and eco-friendly operation. LIBs consists of a positive and a negative electrode separated by an electrolyte solution containing dissociated salts, which enable ion transfer between the two electrodes.[1] Once these electrodes are connected externally, the chemical reactions proceed in tandem at both electrodes, thereby liberating electrons and enabling the current to be tapped by the user. The Fig. 1 illustrates the basic LIB system that leads the current battery market.[2] The main reactions are reversible Li-ion intercalation-de-intercalation cycles between two electrodes.[3] In order to ensure the anodic stability of both the cathode material and the electrolyte solutions, the cathode reactions are:

$$LiCoO_2 \rightleftharpoons Li_{1-x}CoO_2 + xLi^+ + xe^-$$

The first process in the cell is always charging, namely, oxidation and delithiation of $LiCoO_2$ in parallel to the reduction and lithiation of graphite. Graphite intercalates reversibly with lithium to form LiC_6 as the final product according to the following reaction:

$$xC_6 + xLi^+ + xe^- \rightleftharpoons xLiC_6$$

The total equations of chemical reactions during the charge/discharge are as follows.

$$LiCoO_2 + xC_6 \rightleftharpoons Li_{1-x}CoO_2 + xLiC_6$$

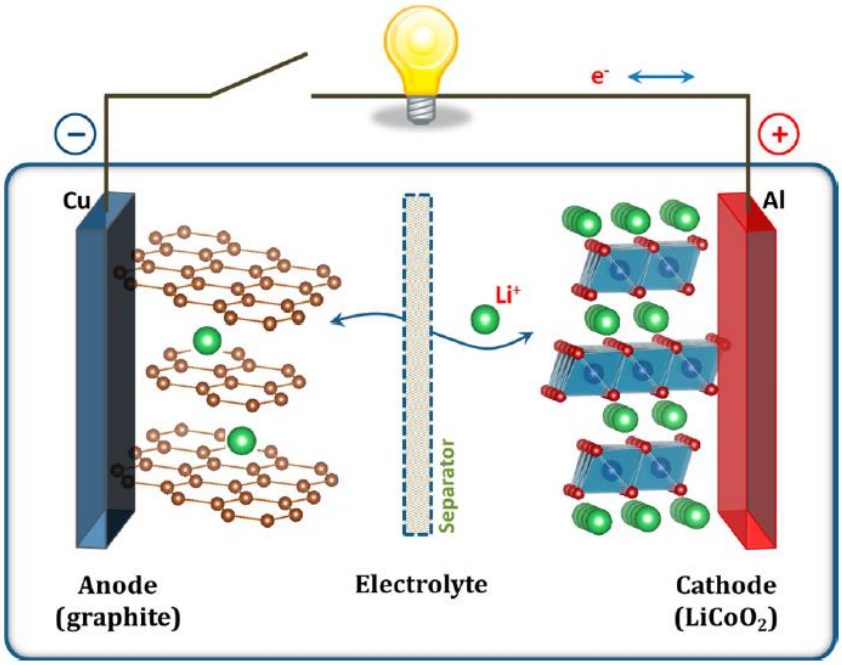

Fig. 1 Schematic illustration of the Lithium-ion battery ($LiCoO_2$/ Li^+ electrolyte/ graphite).[2]

1.2 Issues of Current Lithium based Rechargeable Power Sources

Forthcoming flexible/ wearable electronics, the Internet of Things (IoT), and electric vehicles, which are expected to provide unforeseen ubiquitous connections via electronic transmission, have spurred the relentless pursuit of advanced power sources with reliable electrochemical performance and flexibility.[6, 7] Enormous emphasis should be paid to battery form factors and deformability to achieve this challenging goal, along with continuing efforts in the development of new electrochemically active materials. Meanwhile, from a battery architecture point of view, conventional batteries with fixed shapes and sizes are fabricated by winding or stacking cell components (such as anodes, cathodes, and separator membranes) and then packaging these components into (cylindrical-/rectangular-shaped) metallic canisters or pouch films, followed by liquid-electrolyte injection.[1] Using conventional battery materials and assembly processes, the resulting batteries have limited form factors and mechanical flexibility, thus imposing formidable difficulties for their integration into complex-shaped electronic devices.[8]

In addition, conventional Li rechargeable batteries have solid electrodes and liquid electrolytes, so they suffer from potential risks like volatilization, flammability and explosion. As a result, there is strong demand for safe LIBs. Moreover, it is difficult to effectively improve the energy density of LIBs by applying high voltage cathode materials due to the electrochemical instability of liquid organic electrolytes and separators at high voltage.[9] Solid-state electrolytes could eliminate most of the safety concerns encountered with liquid electrolytes because of their intrinsic solid character. The main advantages of solid-state electrolytes are that they do not corrode, combust, leak or cause internal shorting like their liquid counterparts.[6] Moreover, solid electrolytes are inert toward metallic Li and act as a separator, helping resist to dendrite growth. The important functional properties sought after in an all-solid-state battery include chemical stability in the presence of an anode or high-voltage cathode material, thermal stability during charge and discharge, wide electrochemical stability window against irreversible reaction, and high total Li ionic conductivity.[10]

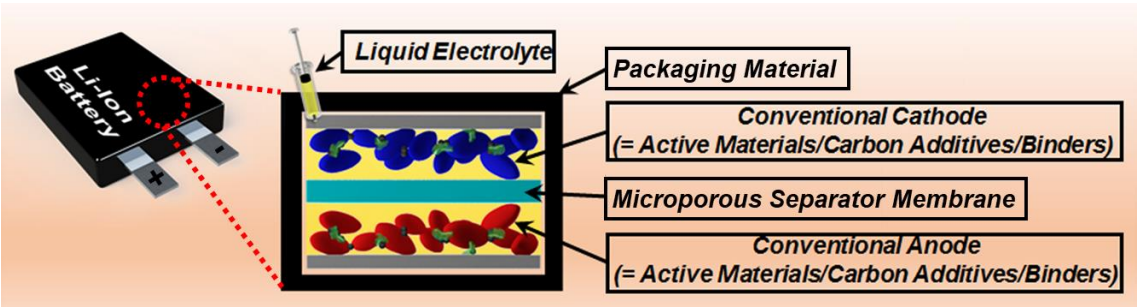

Fig. 2 Schematic illustration of a conventional battery consisting of anode, cathode, microporous separator membrane, and liquid electrolyte inside packaging material with predetermined shape and size.

1.3 References

1. J. -M. Tarascon; M. Armand, Issues and challenges facing rechargeable lithium batteries, Nature, 2001, 414, 359-367.
2. J. B. Goodenough; K. -S. Park, The Li-Ion Rechargeable Battery: A Perspective, J. Am. Chem. Soc., 2013, 135, 1167-1176.
3. V. Etacheri; R. Marom; R. Elazari; G. Salitra; D. Aurbach, Challenges in the Development of Advanced Li-Ion Batteries: A Review, Energy Environ. Sci., 2011, 4, 3243-3262.
4. A. Manthiram; Y. Fu; S. -H. Chung; C. Zu; Y. -S. Su, Rechargeable Lithium-Sulfur Batteries, Chem. Rev., 2014, 114, 11751-11787.
5. D. Peramunage; S. Licht, A Solid Sulfur Cathode for Aqueous Batteries, Science, 1993, 261, 1029-1032.
6. G. Zhou; F. Li; H. -M. Cheng, Progress in flexible lithium batteries and future prospects, Energy Environ. Sci., 2014, 7, 1307-1338.
7. A. Vlad; N. Singh; C. Galande; P. M. Ajayan, Design considerations for unconventional electrochemical energy storage architectures, Adv. Energy Mater., 2015, 5, 1402115.
8. K. -H. Choi; D. B. Ahn; S. -Y. Lee, Current status and challenges in printed batteries: Toward form factor-free, monolithic integrated power sources, ACS Energy Lett., 2018, 3, 220-236.
9. L. Yue; J. Ma; J. Zhang; J. Zhao; S. Dong; Z. Liu; G. Cui; L. Chen, All-solid-state polymer electrolytes for high-performance lithium-ion batteires, Energy Storage Materials, 2016, 5, 139-164.
10. R. Chen; W. Qu; X. Guo; L. Li; F. Wu, The pursuit of solid-state electrolytes for lithium batteries: from comprehensive insight to emerging horizons, Mater. Horiz., 2016, 3, 487-516.

CHAPTER II. Overview of Printed Power Sources

2.1 Printing Technology

In recent years, printing has been used as a fabrication tool for depositing functional inks such as inorganic/organic semiconductors and conductive inks on flexible surfaces to form a new class of electronics that is generally referred to as “printed electronics”. Printing processes offer the advantage of fabricating electronic components over large areas inexpensively as compared to traditional microfabrication techniques.[1]

2.1.1 Printing Techniques

2.1.1.1 Screen-Printing

Screen-printing involves printing inks at a low pressure using a screen mesh containing a designed pattern of uniform thickness. A metal or rubber squeegee can be used for squeezing the thixotropic fluidic ink through the patterned mesh/stencil and onto the substrate. The inks utilized in screen printing have a high viscosity but when forced through the screen mesh/stencil by the squeegee blade, they undergo sheer thinning to facilitate penetration through the screen mesh/stencil which defines the final device pattern. Upon contact with the substrate the ink returns to its viscous state forming the intended shape.[2]

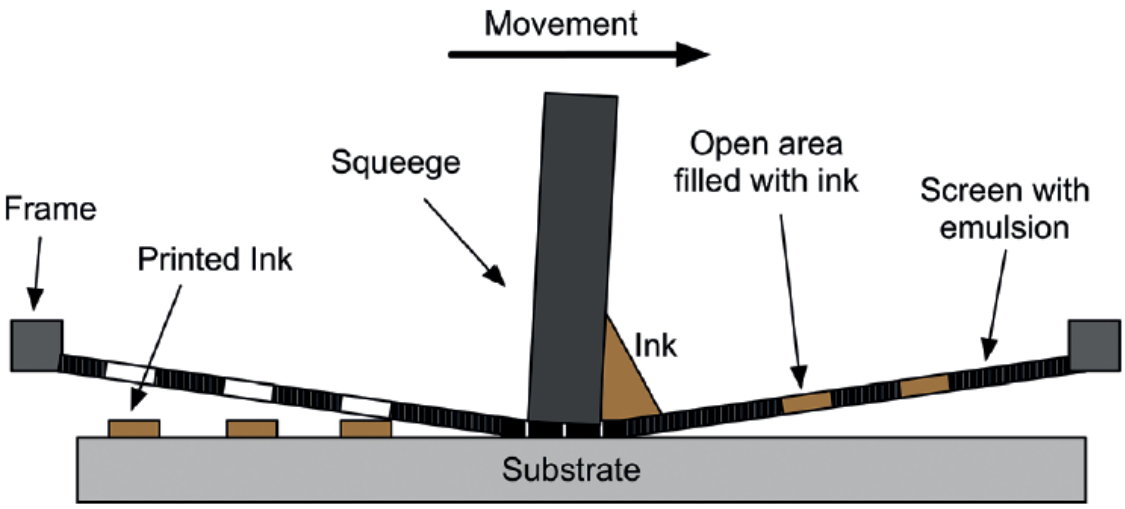

Fig. 3 Schematic illustration of the screen-printing process.[1]

2.1.1.2 Gravure/ Flexography

Gravure/ Flexographic printing is commonly used to print labels for food packaging and corrugated shipping boxes. Flexographic printing has an advantage over lithography due to its facile use of a wider range of inks (spanning from water-based inks to oil-based inks) and compatibility with various substrates such as plastic, foil, paper, and others. Gravure/ flexography transfer the ink to the substrate from an engraved (gravure) or raised (flexography) patterns on a roll. This process is extremely useful for high throughput production of large-area flexible devices.[3]

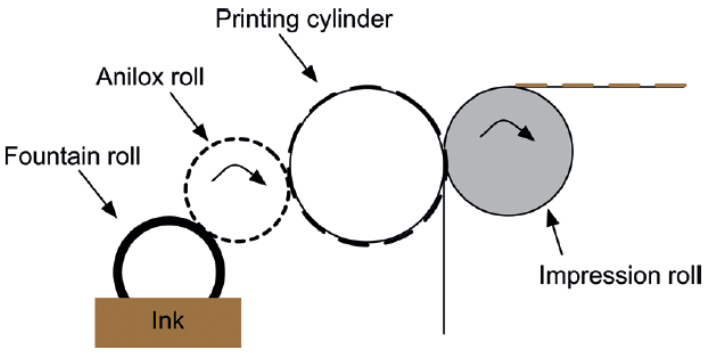

Fig. 4 Schematic illustration of the flexographic printing process.[1]

2.1.1.3 3D/ Inkjet Printing

3D/ Inket printing are a non-contact and additive manufacturing process, can create complex-shaped objects. 3D printing systems consist of ink syringes that deposit inks over substrates. The ink is printed in the form of filaments or drops by modulating the pressure in the ink barrel. Preparing inks for the dispenser printing is more difficult compared to preparations for other printing methods. Inkjet printing is a non-contact, additive-based, and high-precision printing method that does not require the use of predesigned masks and can create versatile patterns through programmable digital files. Inkjet printing requires low-viscosity inks with sufficiently low surface tension to facilitate the jetting process.[3]

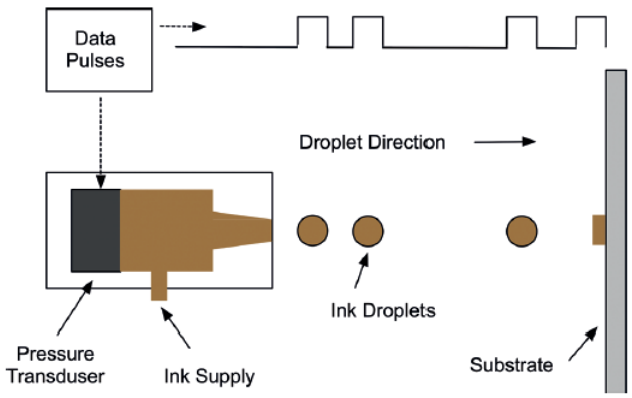

Fig. 5 Schematic illustration of the inkjet printing process.[1]

2.1.2 Printing Requirements

Independent of the printing technique, the common characteristic in all techniques is the use of inks. The ink is thus the main component of the printing techniques. Different printing methods need to use different rheological properties of the ink, so the viscosity ranges of the inks and the obtained thickness of the printed layer should be considering before printing. Ink characteristics also affecting print quality are flow, wetting, and resolubility properties. Typically, the inks for printed batteries are composed of solvent, binder, and a solid component. This solid component consists of one or more components depending the application.[4]

Table 1 shows the most relevant parameters related to the different printing techniques including both ink and printing characteristics. In particular, the ink viscosity is critical in defining printing technique and quality with a range of values for each printing technique. The desired inks should possess excellent printability and satisfy the following requirements. Firstly, the preparation process of the inks should be both uncomplicated and high yield. Secondly, the viscosity and surface tension of printable inks should be located within a suitable range to make them compatible with a variety of printing technologies. Thirdly, the ink should remain stable at room temperature (RT) for months without particle precipitation.[5]

Though tremendous progress has been made in producing inks by using different approaches, it is still a very critical goal in modern materials chemistry and printed electronics research fields and has attracted substantial interest in the last few years. These inks have recently been widely used in the design and manufacture of plastic, textile, and paper substrates-based printed electronics devices, which have become a hotspot in the research into printed electronics.[6]

Table 1. Feature comparison of different printing methods.[2]

Method	Screen-Printing	Gravure/ Flexography	Inkjet	3D/ Dispensing
Viscosity [cP]	500-5000	50-1000	10-20	> 300k
Line Width [μm]	50-100	10-100	10-50	1-100
Line Thickness [μm]	5-250	≤1	≈1-10	1-100
Speed [m/min]	≈70	1000	≈1	<1

2.2 Hetero-colloidal Suspensions

Hetero-colloidal suspensions (solid/liquid dispersions), both of the aqueous and nonaqueous type, find applications in many industrial preparations, of which the following may be worth mentioning: paints, dyestuffs, pigments, paper coatings, printing inks, cosmetics, household products, ceramics, pharmaceuticals and agrochemicals. The control of the properties of these suspensions is critical in the stages involved in their preparation, their long-term stability and in their subsequent application. Some of the parameters which control such properties are: particle size and shape distribution, interparticle interaction forces and the volume fraction of the dispersed phase. These parameters control the flow characteristics (rheology) of these systems.

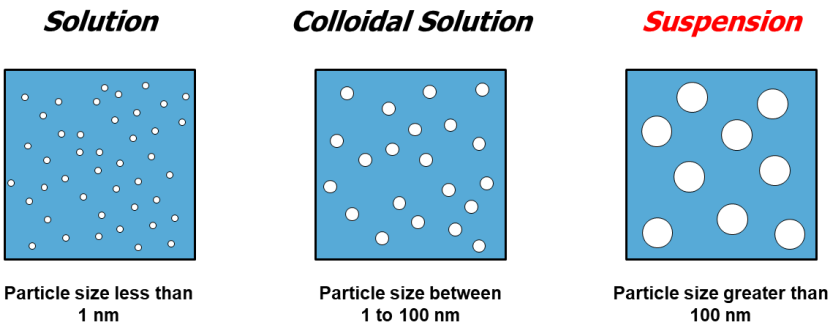

Fig. 6 Three types of solutions.

As the particle number concentration in a suspension is increased, the volume of space occupied by the particles relative to the total volume increases and thus a proportion of space is excluded in terms of its occupancy by any single particle. The probability of particle-particle interaction, both hydrodynamic and surface increases. In this case, the volume fraction is sufficiently high for many-body interaction to occur. Both hydrodynamic and surface interactions play a role in determining the properties of the system.[7]

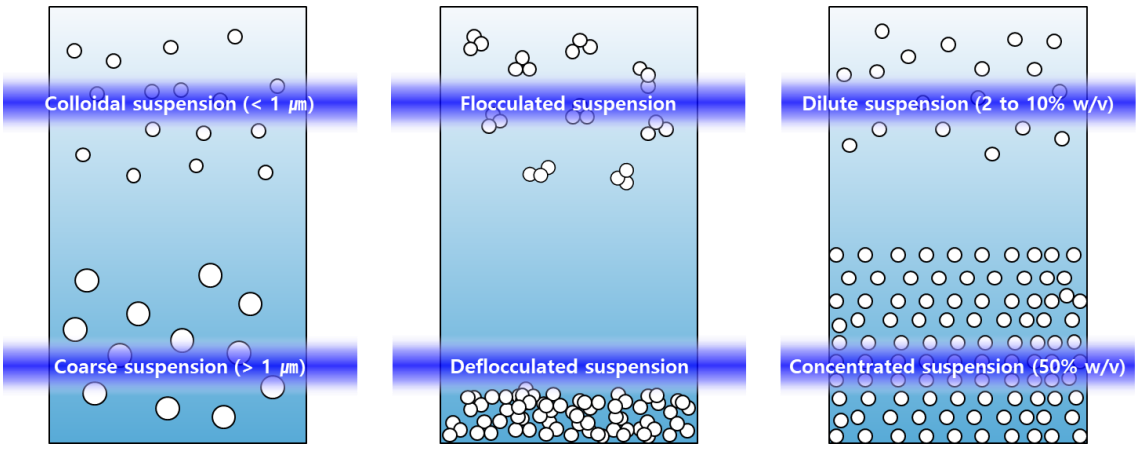

Fig. 7 Classification of suspensions.

2.2.1 Interparticle Interaction

Four different types of interparticle interactions may be identified. The first type of interaction is the so-called “hard-sphere”, which is also sometimes referred to as neutral stability systems, *i.e.* whereby both repulsive and attractive forces are screened.[7] The second type of interaction is that between electrostatically stabilized suspensions with extended double layers (Fig. 8a). Most nanoparticles carry some surface charge in aqueous environments due to the ionization/dissociation of surface groups, or due to the adsorption of charged molecules or ions to the particle surface. The net charge of the system is balanced by the formation of a cloud of counterions around the particle. This cloud is composed of the Stern layer, which consists of counterions adsorbed on the charged surface of the nanoparticles, and the diffuse layer, an atmosphere of ions of opposite net charge surrounding the nanoparticles. Characterization of nanoparticle surface charge is commonly done in terms of the particle zeta potential, which is the electrostatic potential of the particles measured at the so-called shear plane, *i.e.* at the distance from the surface where ions are not bound to the particle. Overlapping electrostatic double layer (EDL)s of two like-particles induces a repulsive force caused by the osmotic interactions between counterions.[8] The third type of interaction is that when the particles possess adsorbed or grafted layers of surfactants and/or macromolecules. In this case, particle interaction occurs as soon as the adsorbed or grafted layers begin to interact. Steric stabilization provides a powerful tool to enhance the dispersion state of NPs under otherwise harsh conditions by preventing two particles from forming attractive vdW interactions due to osmotic pressure and elastic recoil effects (Fig. 8b). Osmotic pressure acts at longer distances, whereas elastic recoil effects dominate at shorter distances. The magnitude of these interactions further depends on the grafting density of the macromolecules to the surface of the particle and its interaction with the dispersion media. However, steric stabilization is only effective if a uniform polymer coating is present on the particle surface. The fourth type of interaction is the van der Waals, which is universal with all disperse systems (Fig. 8c). Generally speaking, the van der Waals attraction between atoms or molecules consists of three main types, namely dipole + dipole (Keesom), dipole-induced dipole (Debye) and dispersion (London) interaction. The most important contribution is the dispersion interaction which occurs between polar and non-polar atoms or molecules. It arises from the charge fluctuation within an atom or molecule associated with the motion of its electrons. The contribution of the van der Waals interaction to the total energy of interaction depends to a large extent on the nature of the particles and medium, the separation distance between the particles and the magnitude of the repulsive force at this separation.

A classical theoretical approach to determine the state of a colloid can be found in the Derjaguin–Landau–Verwey–Overbeek (DLVO) theory. The theory uses the superposition of attractive vdW and repulsive forces caused by the EDL to predict the stability of a colloidal system.

This will be shown in Fig. 8d, when the total interaction between the particles is plotted versus distance of separation between the particles, in which the various contributions are taken into account depending on the stabilization mechanism. These energy-distance curves form the basis of the theories of colloid stability and they also can be used to account for the viscoelastic properties of the suspensions.[7]

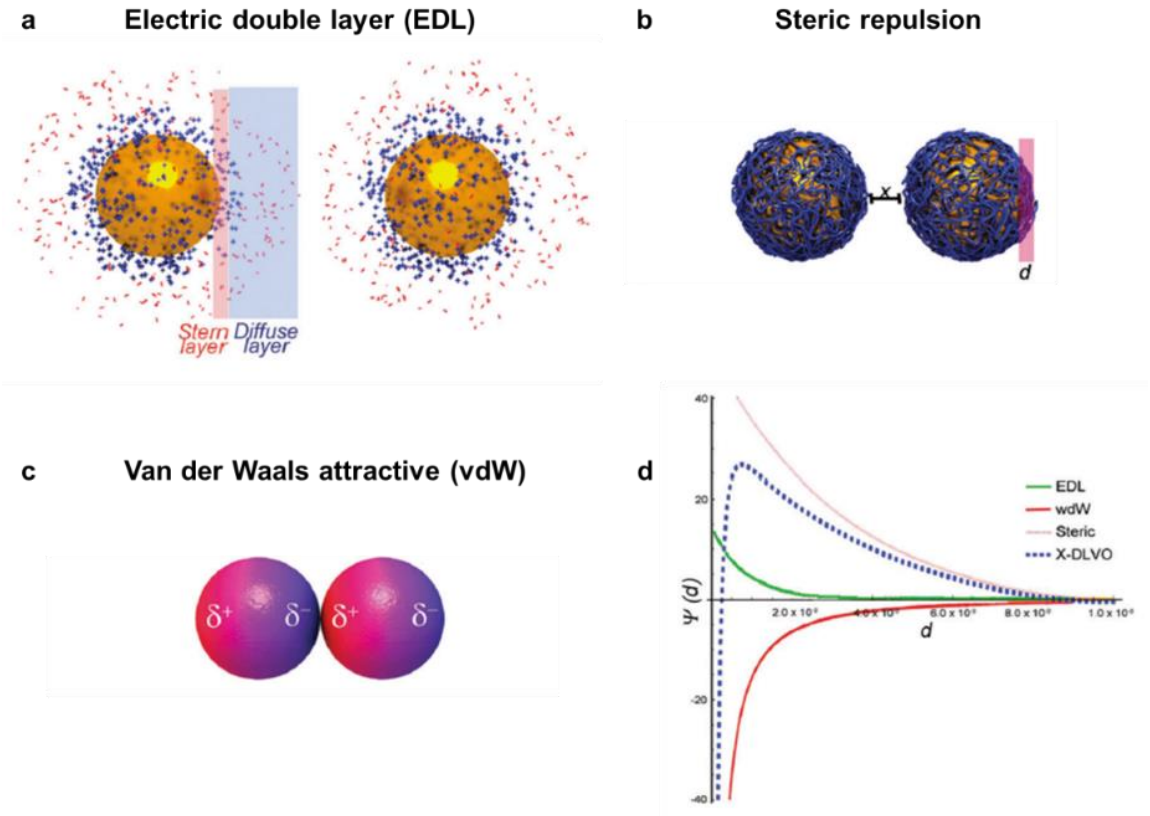

Fig. 8 Colloidal interparticle interactions. (a) electric double layer (EDL), (b) steric repulsion, (c) van der Waals attractive (vdW), (d) illustration of potential energy distance curves.

2.2.2 Suspensions Rheology

Most industrial suspensions show shear-thinning and thixotropic behavior. Highly concentrated suspensions do not exhibit the low shear (Newtonian) plateau depicted by homogenous polymer solutions or melts.[9] In rheology, shear-thinning is the non-Newtonian behavior of fluids whose viscosity (η) decreases under shear strain. Viscosity of a shear-thinning materials is dependent on the degree of the shear load (shear rate or shear stress, respectively). The flow curve shows a decreasing curve slope (Fig. 9a), i.e. viscosity decrease with increasing load (Fig. 9b).

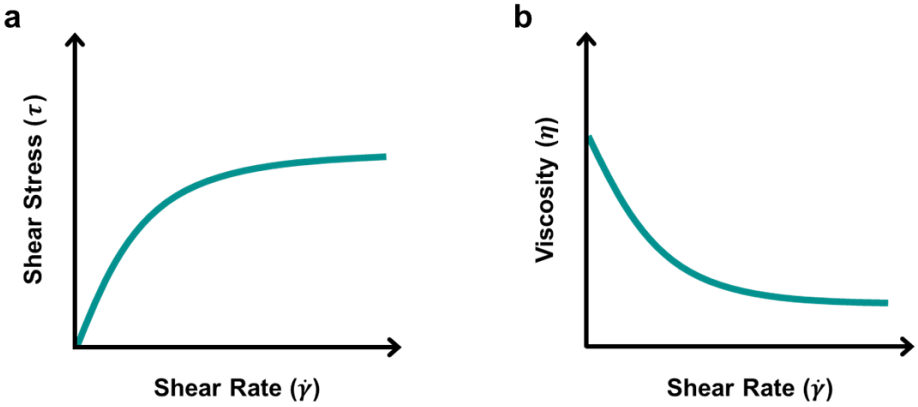

Fig. 9 Shear-thinning flow behavior. (a) Flow curve of a shear-thinning materials, (b) viscosity curve of shear-thinning materials.

Thixotropic fluids are fluids with a variable viscosity which reversibly decreases with time under high shear rates. Because of the reversibility, in general the viscosity increases in time at low or zero shear rates. The usual explanation of thixotropy is that the viscosity of such fluids is mainly caused by the microstructure of for instance particles in the fluid that interconnect and resist large rearrangements. When sheared, this structure is broken down in time and the viscosity consequently decreases in time. When left at rest, the microstructure slowly rebuilds itself and the

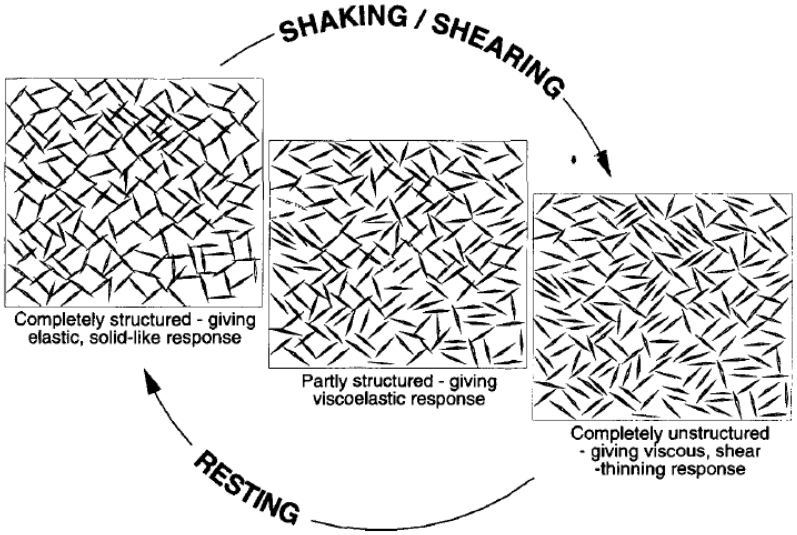

Fig. 10 Breakdown of a 3D thixotropic structure.[11]

viscosity increases.[10] The driving force for microstructural change in flow is the result of the competition between break-down due to flow stresses, build-up due to in-flow collisions and Brownian motion. Brownian motion is the random thermal agitation of atoms and molecules that results in elements of the microstructure being constantly bombarded, which causes them to move to a favourable position where they can-given the necessary attractive force-attach themselves to other parts of the microstructure.[11]

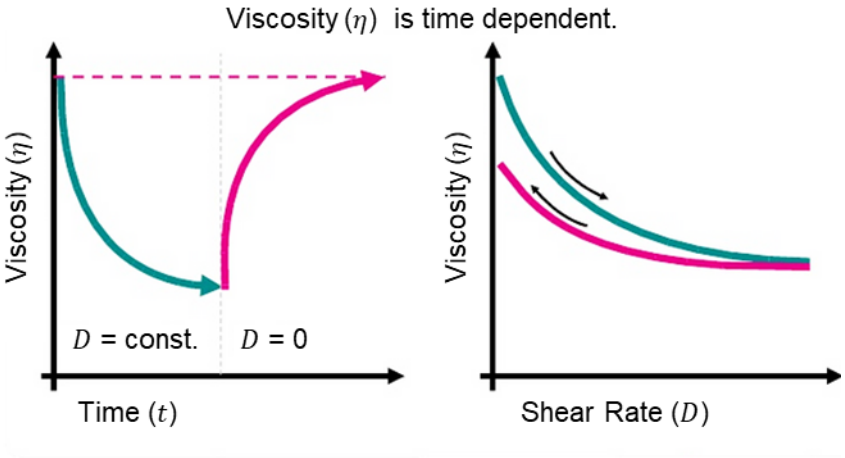

Fig. 11 Rheological properties of thixotropic fluids.

2.3 References

1. A. M. Gaikwad; A. C. Arias; D. A. Steingart, Recent progress on printed flexible batteries: Mechanical challenges, printing technologies, and future prospects, Energy Technol., 2015, 3, 305-328.
2. J. Kim; R. Kumar; A. J. Bandodkar; J. Wang, Advanced materials for printed wearable electrochemical devices: A review, Adv. Electron. Mater., 2017, 1600260.
3. K. -H. Choi; D. B. Ahn; S. -Y. Lee, Current status and challenges in printed batteries: Toword form factor-free, monolithic integrated power sources, ACS Energy Lett., 2018, 3, 220-236.
4. C. Yang; C. P. Wong; M. M. F. Yuen, Printed electrically conductive composites: Conductive filler designs and surface engineering, J. Mater. Chem. C, 2013, 1, 4052-4069.
5. S. B. Walker; J. A. Lewis, Reactive silver inks for patterning high-conductivity features at mild temperatures, J. Am. Chem. Soc., 2012, 134, 1419-1421.
6. W. Wu, Inorganic nanomaterials for printed electronics: A review, Nanoscale, 2017, 9, 7342-7372.
7. T. F. Tadros, Correlation of viscoelastic properties of stable and flocculated suspensions with their interparticle interactions, Adv. Colloid Interface Sci., 1996, 68, 97-200.
8. T. L. Moore; L. R. -Lorenzo; V. Hirsch; S. Balog; D. Urban; C. Jud; B. R. -Rutishauser; M. Lattuada; A. P. -Fink, Nanoparticle colloidal stability in cell culture media and impact on cellular interactions, Chem. Soc. Rev., 2015, 44, 6287-6305.
9. P. J. Carreau; P. A. Lavoie; F. Yziquel, Rheological properties of concentrated suspensions, Rheology Series, 1999, 8, 1299-1345.
10. P. C. F. Møller; J. Mewis; D. Bonn, Yield stress and thixopropy: on the difficulty of measuring yield stresses in practice, 2006, 2, 274-283.
11. H. A. Barnes, Thixopropy – a revies, J. Non-Newtonian Fluid Mech., 1997, 70, 1-33.

CHAPTER III. Printable Solid-State Lithium-Ion Batteries

3.1 Printable Solid-State Bipolar Lithium-Ion Batteries: A New Route toward Shape-Conformable Power Sources with Aesthetic Versatility for Flexible Electronics

3.1.1 Introduction

Rapidly emerging flexible/wearable electronic devices with unusual shape diversity and mobile usability, including wrist-mounted cellular phones, roll-up displays, Google Glass, smart electronic clothing (so-called "e-textiles"), wearable robotic suits and implantable/patchable sensors, draw considerable attention as a kind of disruptive technology to drastically change our daily lives.[1-4] Stimulated by such promising prospect, a number of global electronics makers are fiercely competing to preoccupy this attractive market. To accelerate the advent of the smart electronics era, along with never-ceasing pursuit of high-performance flexible displays and memory chips, development of thin, lightweight and flexible rechargeable power sources should be indispensably required.[5-10]

Among various rechargeable energy storage systems, current state-of-the-art lithium-ion batteries, the most widespread portable power source, could be suggested as a promising solution to fulfill the stringent requirements for flexible electronics.[8-12] From the cell manufacturing point of view, conventional lithium-ion batteries with fixed shapes and sizes are generally fabricated by winding (or stacking) cell components (such as anodes, cathodes and microporous separator membranes) and then packaging them with (cylindrical-/rectangular-shaped) metallic canisters or pouch films, finally followed by injection of liquid electrolytes. In particular, the use of liquid electrolytes gives rise to serious concerns in cell assembly, because they require strict packaging materials to avoid leakage problems and also separator membranes to prevent electrical contact between electrodes.[8,10,13] For these reasons, the conventional cell assembly and materials have pushed the batteries to lack of variety in form factors, thus imposing formidable challenges on their integration into versatile-shaped electronic devices.

The abovementioned design limitation of traditional batteries has spurred us to pay much attention to flexible batteries with shape/design diversity. To date, many of the research works on flexible batteries have been primarily devoted to rational design/synthesis/structural engineering of electrode materials. Details on the previous studies have been comprehensively described in the review articles.[6-10] Some representative achievements include the nanostructured electrode materials based on low-dimensional carbon materials such as carbon nanotube and graphene, and also 3-dimensional (3D) non-metallic current collectors exploiting conductive/compliant papers and textiles.[14-18] Meanwhile, to replace combustible and fluidic liquid electrolytes, which are believed to be a major threat to cell safety and electrolyte leakage failures, solid-state (in particular,

polymer-mediated) electrolytes with balanced electrochemical properties and mechanical flexibility have been demonstrated.[13,19,20]

In addition to these materials-based approaches, a new concept of battery design and architecture, including cable (or fiber)-type and stretchable power systems, have also attracted great interests due to their shape novelty and superior flexibility.[12,18,21-23] Unfortunately, most of the previous works have still relied on traditional cell assembly processes (*i.e.*, winding (or stacking) of electrode sheets and separator membranes → packaging → injection of liquid electrolyte). Meanwhile, in order to address this cell manufacturing-related issues, new fabrication processes such as multi-step spray painting and screen printing processes were recently reported.[24-27] However, they still required the injection step of liquid electrolyte and also a set of mask or screen mesh for spatial alignment of battery components.

Here, as a facile and efficient strategy to resolve the abovementioned deadlocks of conventional battery technologies and also to develop flexible power sources with exceptional shape conformability and aesthetic versatility, we demonstrate a new class of printable solid-state batteries (hereinafter, referred to as "PRISS" batteries). Printing is known to be a simple and reliable technique capable of imparting various surface functionality to a wide diversity of substrates. In particular, stencil printing is one of mass-printing methods, which can be realized by pressing rheologically-tuned inks through a preformed stencil with a squeegee.[28] Recently, besides traditional application fields of printing technology for commodity interests, printed electronics has emerged as an attractive industry due to its process benefits enabling facile fabrication of solution-processable thin-film transistors[28-30] and integrated circuits.[31] In addition, printing concept was exploited in the development of new power sources, although most of which were related to zinc primary batteries. Nylon mesh-embedded Zn electrodes,[32] KOH electrolyte-swelled polyethylene oxide/methyl cellulose gel polymer electrolytes[33] and ionic liquid-swelled polyvinylidene fluoride-hexafluoropropylene gel polymer electrolytes[34] were fabricated via various printing methods. Meanwhile, our group recently reported a bendable and imprintable solid-state composite electrolyte (SCE) as an alternative electrolyte for use in flexible batteries.[20,35]

To fabricate the PRISS batteries, their major components (*i.e.*, SCE layer and SCE matrix-embedded electrodes) are consecutively printed on arbitrary objects of complex design/geometries through simple stencil printing process (followed by ultraviolet (UV) crosslinking). More notably, this printing process for PRISS batteries does not require traditional processing solvents such as acetone, water and N-methyl pyrrolidone (that are essentially used for preparation of conventional electrodes/self-standing polymer electrolyte films and also demand time-/energy-consuming drying processes), liquid-electrolyte injection and conventional microporous separator membranes, eventually leading to the fabrication of fully-integrated,

multilayer-structured PRISS batteries with shape conformability and design universality far beyond those accessible with conventional cell components and manufacturing processes. Furthermore, such process simplicity and scalability of PRISS batteries allow seamless integration into complex-shaped electronic devices, thus enabling the realization of power source-unitized electronics. We anticipate that PRISS batteries hold a great deal of promise as a versatile and scalable platform technology to overcome battery-triggered design issues facing flexible/wearable electronic gadgets.

3.1.2 Experimental

3.1.2.1 Design and Fabrication of PRISS Cells

To fabricate printable electrodes, the SCE matrix precursor, which was composed of UV-curable ETPTA monomer (incorporating 1.0 wt.% HMPP as a photoinitiator) and high boiling point electrolyte (1M $LiPF_6$ in EC/PC = 1/1 v/v) wherein the composition ratio of ETPTA/high boiling point electrolyte = 15/85 (w/w), was mixed with electrode active materials (here, LFP (Süd Chemie) and LTO (Süd Chemie) powders were chosen) and carbon black conductive additives. The weight-based composition ratios of electrode slurry mixtures were electrode active powders/carbon black/SCE matrix precursor = 38/4/58 (w/w/w) for LFP cathode and 27/7/66 (w/w/w) for LTO anode, respectively. The LTO anode slurry was printed on an Al current collector using stencil printing technique (copper foil-based stencils with various shapes/thickness were used) without using any processing solvents such as NMP or water and then exposed to UV irradiation for a short time less than 30 sec, yielding the printable LTO anode. The UV irradiation was performed using a Hg UV-lamp (Lichtzen), with an irradiation peak intensity of approximately 2000 mW cm^{-2} on the sample surface. Subsequently, on top of the LTO anode, the SCE paste (ETPTA/1M $LiPF_6$ in EC/PC/Al_2O_3 nanoparticles (average particle size ~ 300 nm) = 5/28/67 w/w/w) was introduced via the same stencil printing and UV curing process, leading to a solid-state SCE thin layer on the LTO anode. Then, the LFP cathode slurry was printed directly on the SCE layer/LTO anode unit and subjected to UV irradiation. After placing Al current collector on top of the printable LFP cathode/printable SCE layer/printable LTO anode (C/S/A) assembly, a full-integrated and multilayer-structured PRISS cell was finally obtained.

3.1.2.2 Structural/Rheological/Physical Characterization of PRISS Cells

The UV curing reaction of the printable cell components such as cathode, anode and electrolyte were examined using a FT-IR spectrometer (FT-3000, Excalibur) with a spectral resolution of 4 cm^{-1}. The morphologies (cross-sectional view) of the printable cell components were characterized by field emission scanning electron microscopy (FE-SEM, Hitachi) equipped with energy-dispersive spectrometer (EDS). The rheological properties of the printable cell components were measured with a rheometer (Haake MARS 3, Thermo Electron GmbH). The physical flexibility of the printable cell components upon mechanical deformation such as folding and winding (rod diameter = 5 mm) was also investigated.

3.1.2.3 Electrochemical Analysis and Shape Conformability/Printability of PRISS Cells

To elucidate basic electrochemical performance of PRISS batteries (including half cells), a unit cell (2032-type coin) was prepared in an argon-filled glove box. The cell performance was measured using a cycle tester (PNE Solution) at various charge/discharge conditions. To explore potential applicability of PRISS batteries as a shape-conformable power source with aesthetic versatility, the PRISS cells were fabricated directly on paper (Hi-Q ACB, HANSOL PAPER Co., Korea)-made eyeglasses and a transparent glass cup using the abovementioned stencil printing and UV-curing process. Here, to visualize the unique architecture of PRISS cells, a transparent PDMS-coated PE film (thickness ~ 100 μm) was prepared and employed as a flexible packaging material. Also, the "PRISS" letters-shaped PRISS cell was fabricated through the stencil printing-based manufacturing process. To understand electronic/ionic transport phenomena of PRISS cells, with a particular focus on electrochemical behavior inside electrodes, the EIS (VSP classic, Bio-Logic) analysis was performed using symmetric cells with two different modes (non-blocking vs. blocking) over a frequency range of 10^{-1} to 10^{6} Hz.

3.1.3 Results and Discussion

3.1.3.1 Architecture design and Fabrication

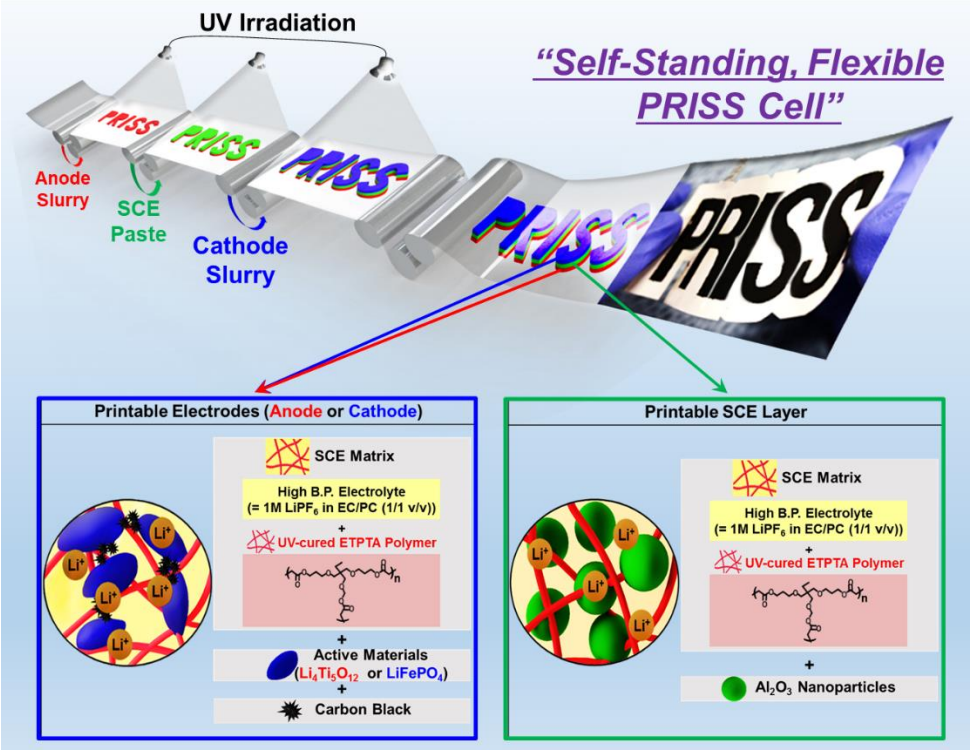

Fig. 12 Schematic representation depicting the stepwise fabrication procedure for PRISS cells, wherein chemical structure of their major components and a photograph of the self-standing, flexible "PRISS" letters-shaped PRISS cell were provided.

The stepwise fabrication procedure (potentially being combined with roll-to-roll process in future works) for PRISS cells, along with chemical structure of their major components, was depicted in a schematic representation (Fig. 12). The SCE matrix precursor, which was composed of UV-curable ethoxylated trimethylolpropane triacrylate (ETPTA) monomer[20,35] (incorporating 1.0 wt.% 2-hydroxy-2-methyl-1-phenyl-1-propanone (HMPP) as a photoinitiator) and high boiling point electrolyte (1M $LiPF_6$ in ethylene carbonate (EC, b.p. = 261 °C)/propylene carbonate (PC, b.p. = 242 °C) = 1/1 v/v) wherein the composition ratio of ETPTA/high boiling point electrolyte = 15/85 (w/w), was mixed with electrode active materials (here, $LiFePO_4$ (LFP, cathode) and $Li_4Ti_5O_{12}$ (LTO, anode) powders were chosen as model electrode active materials to explore the proof of concept for PRISS cells) and carbon black conductive additives. The EC/PC-based electrolyte shows good thermal stability due to its high boiling point/low vapor pressure.[20,35] The weight-based composition ratios of electrode slurry mixtures (= electrode active powders/carbon black/SCE matrix precursor) were respectively 38/4/58 (w/w/w) for LFP cathode and 27/7/66 (w/w/w) for LTO anode.

The LTO anode slurry was printed on an aluminum (Al) current collector using stencil printing technique (here, copper foil-based stencils with various shapes/thickness were used) and then exposed to UV irradiation for a short time less than 30 sec, leading to the SCE matrix-embedded solid state LTO anode. Subsequently, on top of the LTO anode, the SCE paste (ETPTA/high boiling point electrolyte/Al_2O_3 nanoparticles (average particle size ~ 300 nm) = 5/28/67 w/w/w) was introduced via the same stencil printing and UV curing process, yielding a printable SCE thin layer (acting as a separator membrane as well as solid state electrolyte) on the LTO anode. Then, the LFP cathode slurry was stencil printed directly on the SCE layer/LTO anode unit and subjected to UV irradiation. After placing Al current collector on top of the printable LFP cathode/printable SCE layer/printable LTO anode (C/S/A) assembly, a full-integrated and multilayer-structured PRISS cell was finally obtained. More details on the stencil printing-based cell fabrication procedure were described in the experimental section. A photograph of the self-standing, flexible "PRISS" letters-shaped PRISS cell is also presented in Fig. 12.

The PRISS cell, as compared to a conventional cell that consists of anode, cathode, microporous separator membrane and liquid electrolyte inside a packaging material with pre-determined shape and size, offers the following composition/processing benefits: (i) being free from conventional microporous separator membranes and polymeric binders such as polyvinylidene fluoride (PVdF) or carboxymethylcellulose (CMC)/styrene-butadiene rubber (SBR) in the electrodes, thereby enabling the removal of time-/cost-consuming drying of processing solvents (*i.e.*, N-methyl-2-pyrrolidone (NMP), water and so on); (ii) no extra step for liquid-electrolyte injection.

3.1.3.2 Designing Printable Electrode/Electrolyte Suspensions and Their Structural/Rheological/Physicochemical Uniqueness

A key technology to enable the realization of PRISS cells is the fine-tuning of rheological properties of electrode slurries and SCE pastes, in addition to the material uniqueness of basic elements. As a control sample, a conventional electrode slurry (for example, LFP/carbon black additive/PVdF binder = 80/10/10 (w/w/w) in NMP, solid content in the electrode slurry = 35 wt.%) was chosen. The electrode slurry tends to flow downward when it is vertically placed on an Al current collector (Fig.13a). The electrode slurry shows the relatively low viscosity (~ 200 Poise) and also the less steep decrease in viscosity with shear rate. Moreover, the storage modulus (G') was found to be lower than the loss modulus (G") over a wide range of shear stress. Elaborate works may resolve the rheology problems mentioned above, however, a critical drawback of conventional electrode slurries is that they essentially require extra time-/energy-consuming steps for removal of processing solvents (such as NMP or water) and also injection of liquid electrolyte (used for activating ionic conduction inside electrodes).

By contrast, for the PRISS cells, the printable LFP cathode slurry (LFP/carbon black/SCE matrix precursor = 38/4/58 (w/w/w) without NMP solvent) presents significantly higher viscosity (~ 2.3 x 10^5 Poise) and also non-Newtonian fluid (specifically, shear-thinning) behavior (Fig. 13b).

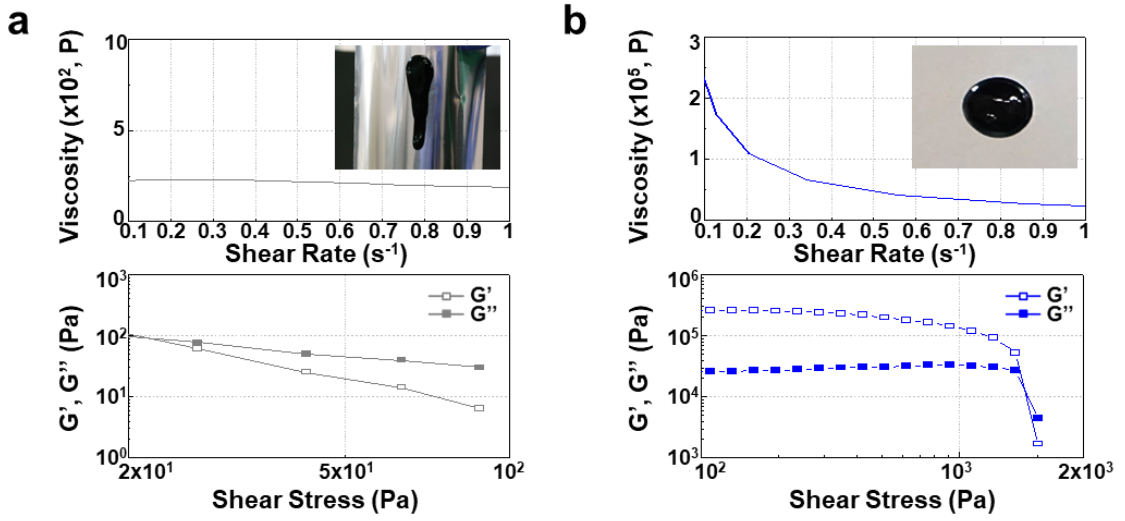

Fig. 13 (a) Rheological properties (viscosity and viscoelasticity represented by storage modulus (G') and loss modulus (G")) of a conventional LFP slurry (LFP/carbon black additive/PVdF binder = 80/10/10 (w/w/w) in NMP, solid content of the cathode slurry = 35 wt.%). (b) Rheological properties of printable LFP cathode slurry (LFP/carbon black additive/SCE matrix precursor = 38/4/58 (w/w/w) without NMP solvent).

The viscoelastic analysis of the printable LFP cathode slurry shows that G' is higher than G" at low shear stress region and the opposite trend is observed at high shear stress region. Similar rheological behavior was also observed at the LTO anode slurry (LTO/carbon black additive/SCE matrix precursor = 27/7/66 (w/w/w) without NMP solvent) (Fig. 14).

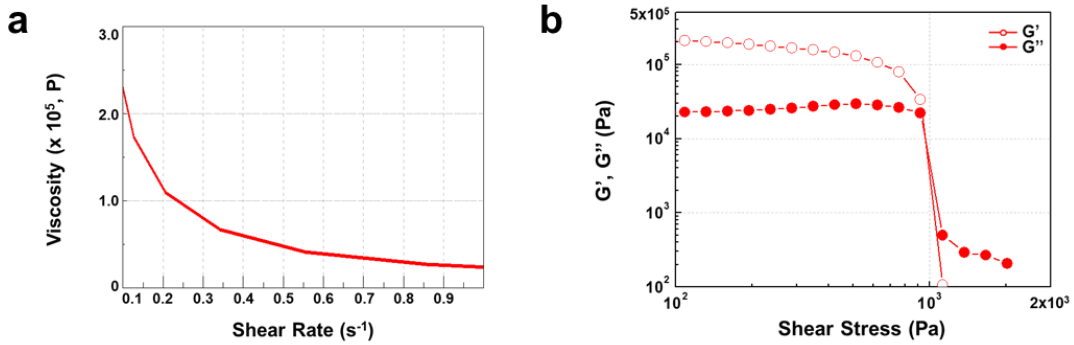

Fig. 14 Rheological properties of printable LTO anode slurry (LTO/carbon black additive/SCE matrix precursor = 27/7/66 (w/w/w) without NMP solvent) for a PRISS cell: (a) viscosity; (b) storage modulus (G') and loss modulus (G").

The abovementioned rheology results of the electrode slurries verify a typical thixotropic fluid behavior.[36,37] Effect of the solid (= LFP powders + carbon black additives) content in the printable LFP cathode slurries on their rheological properties was investigated. In comparison to the optimized solid content ((LFP + carbon black) = 42 wt.%), the lower solid content (= 20 wt.%, the LFP/carbon black composition ratio was identical to that of the optimized solid content) in the electrode slurry reduced the viscosity and also weakened the thixotropic fluid characteristic (Fig. 15a, b). Meanwhile, the higher solid content (= 50 wt.%) failed to secure good dispersion state in the cathode slurry, giving rise to serious agglomeration of particles (Supporting Information Fig. 15c). These results underscore the importance of rheology control in fabricating the printable electrodes.

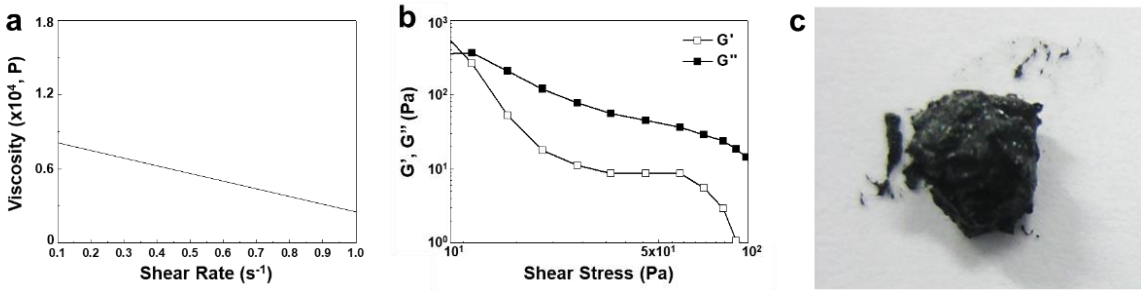

Fig. 15 Effect of solid content (= LFP powders + carbon black) in printable LFP cathode slurries on rheological properties. At lower solid content (= 20 wt.%): (a) viscosity; (b) storage modulus (G') and loss modulus (G"). At higher solid content (= 50 wt.%): (c) a photograph showing the poor dispersion state (*i.e.*, serious agglomeration of particles) in the cathode slurry.

With the optimized composition ratios of electrodes (LFP/carbon black/SCE matrix precursor = 38/4/58, LTO/carbon black/SCE matrix precursor = 27/7/66 w/w/w), the self-standing electrodes containing the solid state electrolytes were directly fabricated via the stencil printing followed by UV curing process. The cross-sectional scanning electron microscopy (SEM) and energy dispersive spectroscopy (EDS) images (Fig. 16) show that the electrode active materials and carbon black additives are densely packed and also well dispersed in the through-thickness direction. Notably, the highly-percolated nanoscale interstitial voids formed between the electrode active materials and carbon black additives, corresponding to the space originally occupied by the EC/PC-based liquid electrolyte that was selectively removed using dimethyl carbonate (DMC, as an etching solvent) prior to the SEM analysis, indicate the construction of ion-conductive pathways[20,35] in the printable electrodes. In addition, the good dispersion state of LFP particles and carbon black additives was observed, revealing the formation of electronic networks in the printable electrodes. These electronic networks, in combination with the ionic channels mentioned above, are expected to play important roles in enabling normal Faradaic reactions in the printable electrodes.

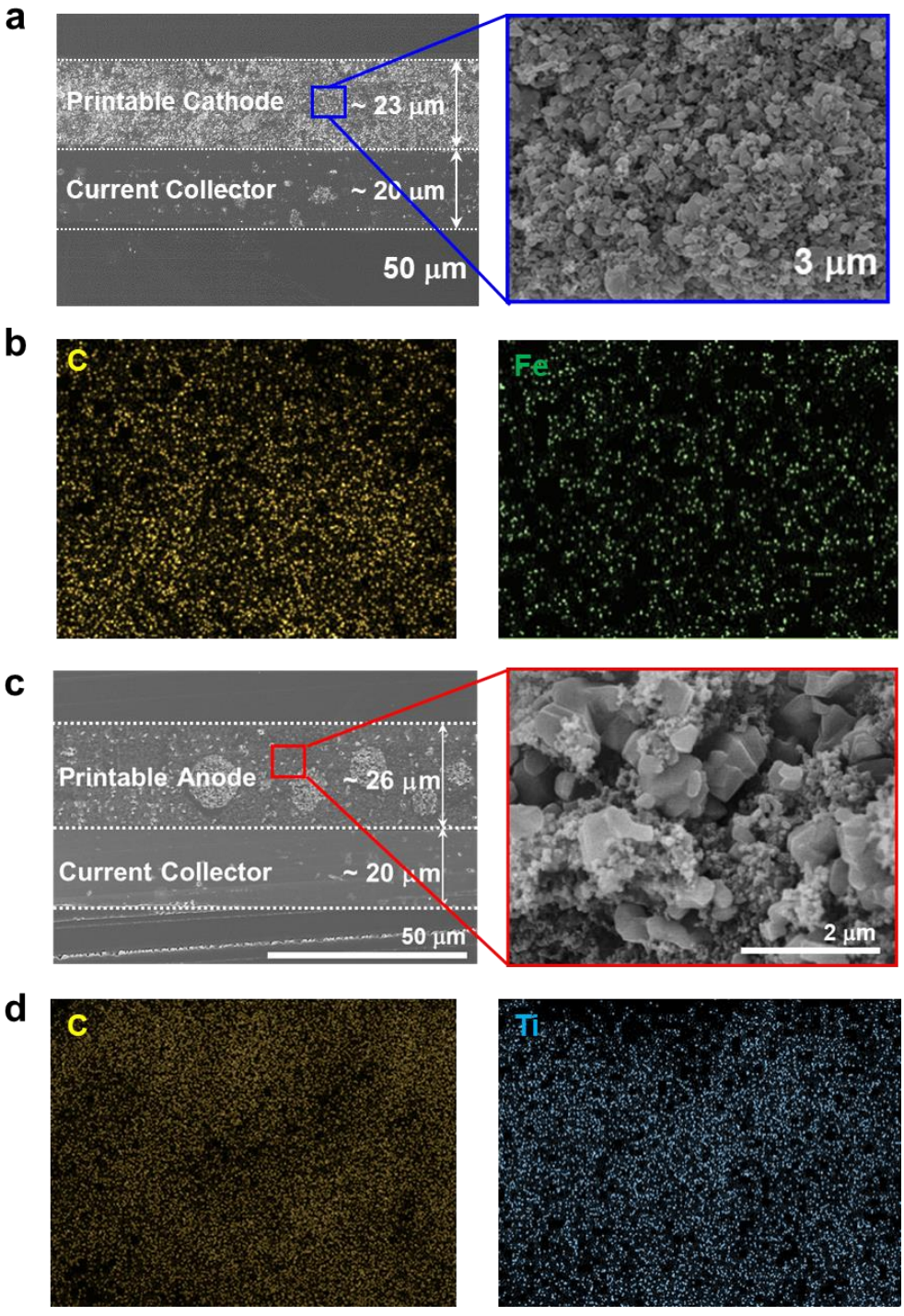

Fig. 16 Morphological characterization (cross-sectional view) of printable electrodes, LFP cathode: (a) SEM images; (b) EDS images, LTO anode: (c) SEM images; (d) EDS images.

The FT-IR analysis (Fig. 17) shows that the characteristic peaks corresponding to acrylic C=C bonds (1610 - 1625 cm^{-1})[13,19,35] of ETPTA monomer disappeared after exposure to UV irradiation, demonstrating that the ETPTA monomer was photo-polymerized in the printable electrode slurry. In addition, gel content (*i.e.*, insoluble polymer fraction after solvent (DMC → acetone) extraction) of the printable electrodes was observed to be higher than 99 %, confirming the successful UV curing reaction of ETPTA monomer.

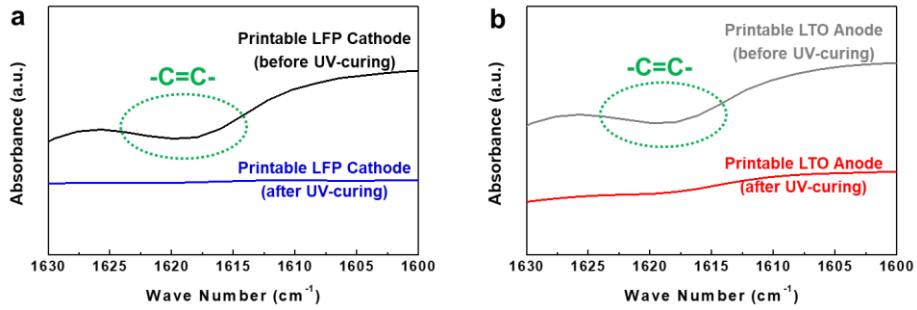

Fig. 17 Change in the FT-IR spectra of acrylic C=C double bonds of ETPTA before/after UV irradiation: (a) printable LFP cathode; (b) printable LTO anode.

Fig. 18 shows that the self-standing printable electrodes are not mechanically disrupted upon physical deformation such as folding and winding (rod diameter = 5 mm). This result underscores unique functions of the SCE matrix (comprising UV-cured ETPTA polymer and EC/PC-based liquid electrolyte) serving as an alternative binder as well as solid state electrolyte, which brings the good dimensional/mechanical robustness even in the absence of traditional polymeric binders such as PVdF or CMC/SBR. The aforementioned thixotropic fluid behavior of printable electrode slurries allows the fabrication of SCE matrix-embedded electrodes having various form factors. Fig. 18b shows that the letters-shaped LFP cathode slurry (represented by a word of "UNIST") can be directly printed on an Al current collector, prior to UV curing. By comparison, the conventional LFP cathode slurry failed to maintain the letter form when it was tilted toward vertical position.

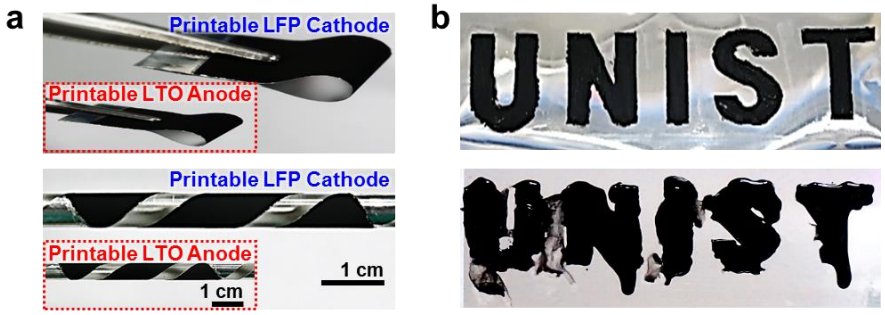

Fig. 18 (a) Photographs showing mechanical flexibility of printable electrodes upon physical deformation such as folding and winding (rod diameter = 5 mm). (b) Photographs of the letters-shaped LFP cathode slurry (represented by a word of "UNIST", upper image)

In addition to the letters-shaped electrodes, by exploiting UV IL (imprint lithography) technique,[20,35] the microstructure-patterned electrodes were produced. The LFP cathode slurry cast on an Al current collector was pressed by a microscale stripe-patterned polydimethyl siloxane (PDMS) stamp and then exposed to UV irradiation through the transparent PDMS stamp side, leading to a self-standing SCE matrix-embedded LFP cathode with inverse replica of the finely-defined microscale stripe pattern (Fig. 19). A schematic illustration depicting the UV IL-driven micropatterning technique was also provided. These results demonstrate that the printable electrode strategy offers unprecedented opportunity in developing the solid state electrolyte-embedded electrodes with tunable/versatile shapes and sizes.

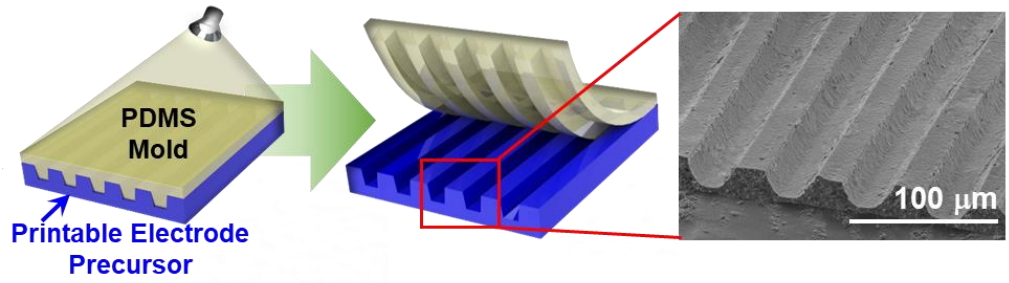

Fig. 19 A schematic illustration of the UV-IL technique-driven micropatterning procedure and a SEM photograph showing the printable LFP cathode with inverse replica of the finely-defined microscale stripe pattern.

In the PRISS cells, another important component is the printable SCE layer (= UV-cured ETPTA polymer/1M $LiPF_6$ in EC/PC/Al_2O_3 nanoparticles).[20,35] Here, the Al_2O_3 nanoparticles act as a multifunctional filler to control thixotropic fluid behavior of SCE pastes and also impart the resulting SCE layers with dimensional stability/mechanical robustness. Major characteristics of the printable SCE layers, including rheological properties (in terms of viscosity and viscoelasticity), microscale imprintability, mechanical flexibility and ionic conductivity were investigated and summarized in Fig. 20.

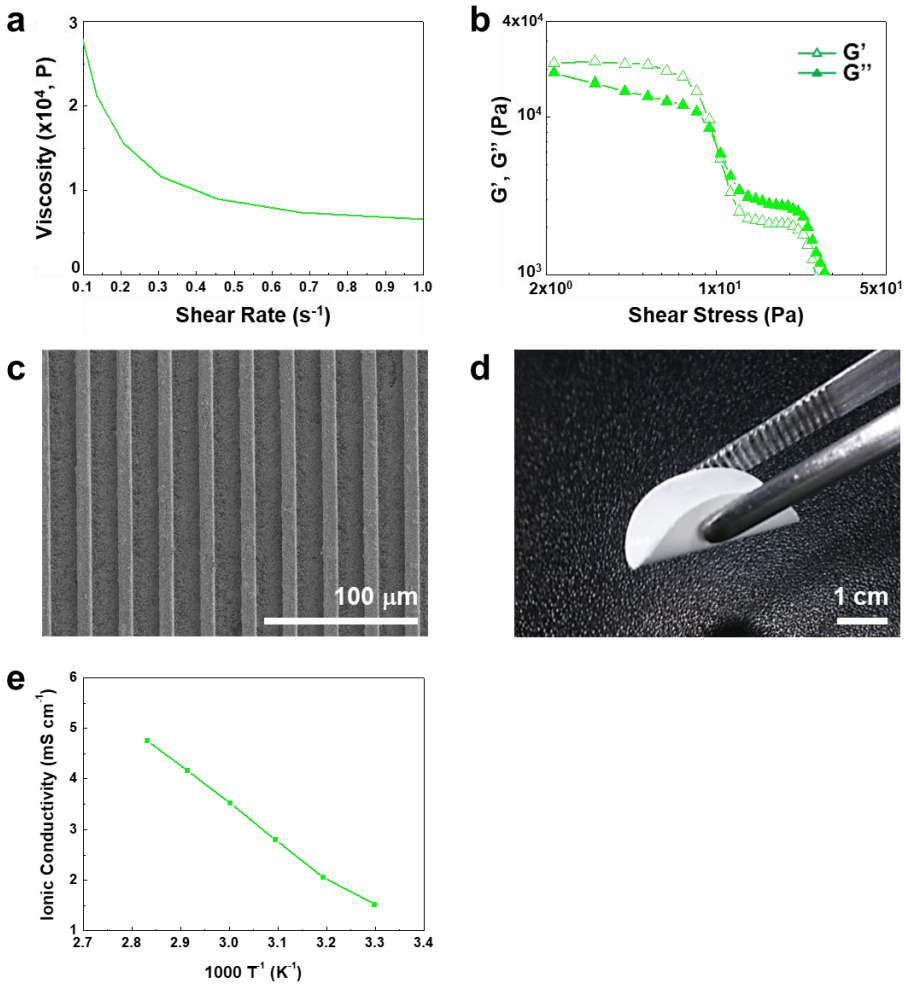

Fig. 20 Major characteristics of printable SCE layers: (a) viscosity; (b) G' and G"; (c) microscale imprintability; (d) mechanical flexibility; (e) temperature-dependent ionic conductivity.

3.1.3.3 Electrochemical Performance and In-Depth EIS Analysis of PRISS Cells

Based on the understanding of structure and physicochemical properties of printable electrodes and printable SCE layers, electrochemical performance of PRISS cells was investigated in terms of their charge/discharge behavior. Fig. 21a shows charge/discharge profiles of a LFP half cell (= printable LFP cathode/(1M $LiPF_6$ in EC/PC)-soaked polyethylene (PE) separator/lithium metal anode) as a function of cycle number. The cell was cycled at a fixed charge/discharge current density of 0.1 C (= 0.05 mA cm^{-2})/0.1 C under a voltage range of 2.5 - 3.8 V. No abnormal charge/discharge behavior was observed with cycling, demonstrating the electrochemical validity of the printable LFP cathode. The half-cell performance of a printable LTO anode was also examined (Fig. 21b). Similar to the results of the printable LFP cathode, the printable LTO anode showed stable charge/discharge cycling behavior.

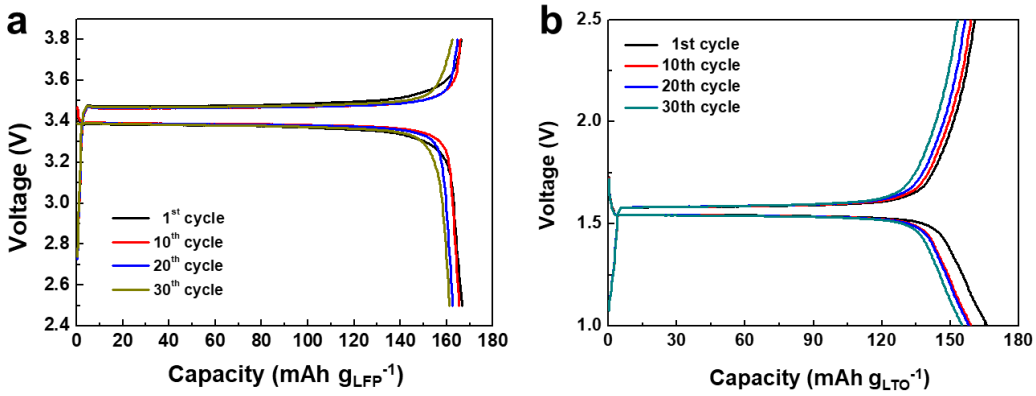

Fig. 21 Galvanostatic charge/discharge profiles of (a) LFP half cell (= printable LFP cathode (LFP/carbon black/SCE matrix = 38/4/58 w/w/w)/(1M LiPF6 in EC/PC)-soaked PE separator/lithium metal anode) as a function of cycle number, wherein the PE separator was previously treated by 1N H_2SO_4 solution to facilitate the uptake the EC/PC-based liquid electrolyte. The cell was cycled at a fixed charge/discharge current density of 0.1 C/0.1 C under a voltage range of 2.5 - 3.8 V, where the gravimetric charge/discharge capacity was estimated based on the mass of LFP active materials, (b) LTO half cell (= printable LTO anode (LTO/carbon black/SCE matrix = 27/7/66 w/w/w)/(1M $LiPF_6$ in EC/PC)-soaked PE separator/lithium metal anode) as a function of cycle number, where the PE separator was previously treated by 1N H_2SO_4 solution to facilitate the uptake EC/PC-based liquid electrolyte. The cell was cycled at a fixed charge/discharge current density of 0.1 C/0.1 C under a voltage range of 1.0 - 2.5 V, where the gravimetric charge/discharge capacity was estimated based on the mass of LTO active materials.

After elucidating the half-cell performance of each printable electrode, a PRISS full cell (composed of the printable LTO anode, printable SCE layer and printable LFP cathode) was fabricated and its electrochemical performance was analyzed. A cross-sectional SEM image (Fig. 22a) shows that a PRISS full cell (= printable LFP cathode (~ 34 μm, excluding Al current collector)/printable SCE layer (~ 60 μm)/printable LTO anode (~ 25 μm)) was successfully constructed, wherein the EC/PC-based liquid electrolyte was removed prior to the SEM analysis. Neither structural instability nor delamination between the electrodes and SCE layer was observed in the PRISS cell.

The electrochemical performance of the PRISS full cell was examined at room temperature (Fig. 22b), where the cell was cycled between 1.0 and 2.5 V at a constant charge/discharge current density (= 0.05 C/0.05 C). The PRISS full cell presents normal charge/discharge profiles and also stable capacity retention (~ 90 %) up to 30 cycles, even without injection of extra liquid electrolyte and conventional microporous separator membranes. The structural stability of the PRISS full cell after the cycling test (30 cycles) was investigated. The full-integrated multilayer structure was well preserved in overall and neither morphological disruption nor local structural defects were found at the printable electrodes (Fig. 22c).

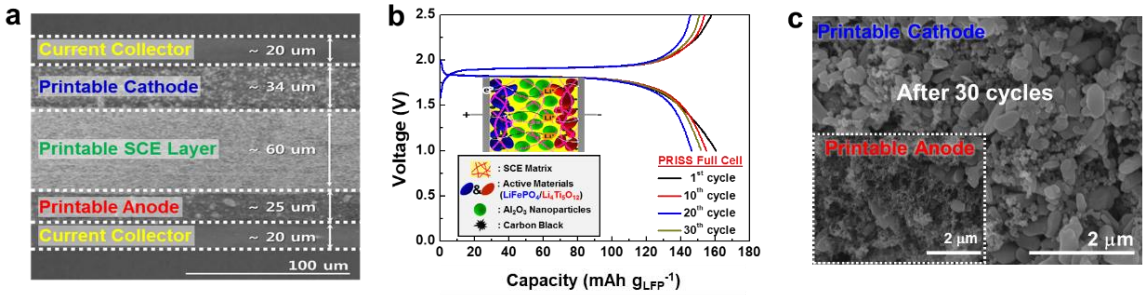

Fig. 22 (a) A SEM image (cross-sectional view) of a PRISS full cell (= printable LFP cathode (LFP/carbon black/SCE matrix = 38/4/58 w/w/w)/printable SCE layer (ETPTA/1M $LiPF_6$ in EC/PC/Al_2O_3 nanoparticles = 5/28/67 w/w/w)/printable LTO anode (LTO/carbon black/SCE matrix = 27/7/66 w/w/w)), wherein the EC/PC-based liquid electrolyte was removed prior to the SEM analysis. (b) Galvanostatic charge/discharge profiles of a PRISS full cell as a function of cycle number. The cell was cycled between 1.0 and 2.5 V at a constant charge/discharge current density (= 0.05 C/0.05 C), where gravimetric charge/discharge capacity was estimated based on the mass of LFP active materials. (c) SEM images (cross-sectional view) of the printable electrodes after the cycling test (30 cycles).

3.1.3.4 Shape Conformability, Aesthetic Versatility and Printability of PRISS Cells: Toward a Reliable Power Source for Forthcoming Flexible/Wearable Electronic Devices

Currently available batteries with traditional designs and shapes (in most cases, cylindrical, prismatic and pouch types) have critical limitations in developing power source-unitized electronics (left image of Fig. 23). To facilitate the advent of flexible/wearable electronics era, the power systems need to be shape-conformable and also seamlessly integrated with electronic devices (right image of Fig. 23). In this respect, PRISS cells could be suggested as a promising candidate to power next-generation flexible/wearable electronic devices.

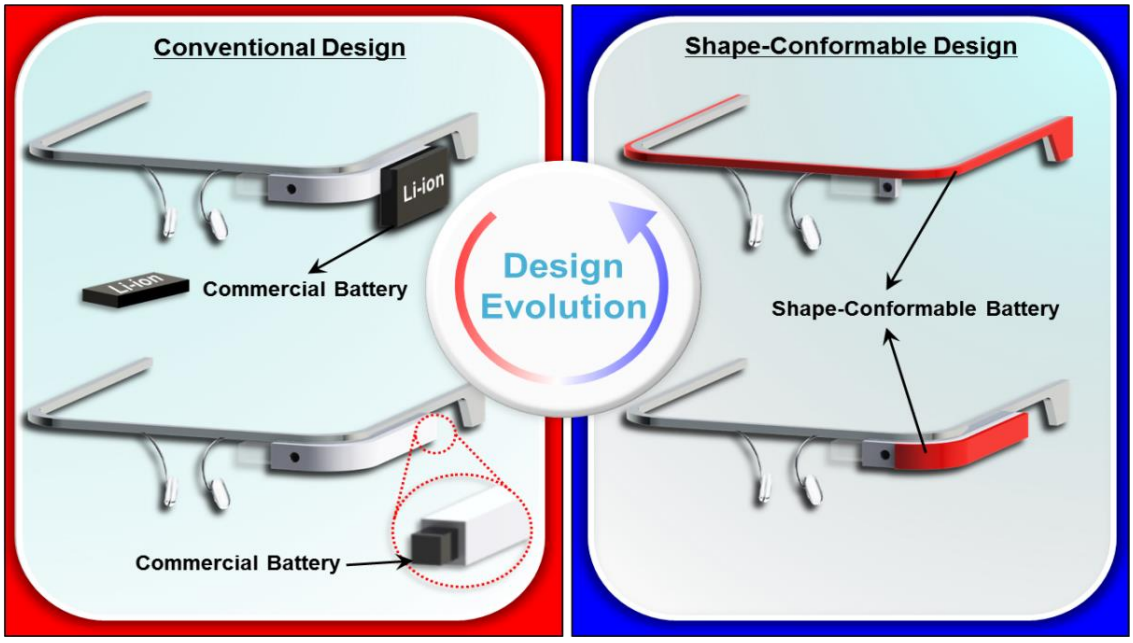

Fig. 23 Conceptual comparison of cell design and shape (left image = conventional cell, right image = PRISS cell that can be shape-conformable and also seamlessly integrated with electronic devices).

To explore the applicability of PRISS cells, we prepared paper-made eyeglasses as a kind of Google Glass-mimic ones and then fabricated the PRISS cell directly on top of the paper-made eyeglasses. The components and composition ratio of the PRISS cell were the same as those provided in Fig. 22. Onto one side (Al foil was pre-attached as a current collector) of the paper-made eyeglasses, the LTO anode slurry (comprising LTO/carbon black/SCE matrix precursor) was printed and exposed to UV irradiation. Subsequently, the SCE layer was introduced onto the printable LTO anode. Finally, the LFP cathode was printed on top of the printable SCE layer/printable LTO anode assembly. During the whole printing-based fabrication steps (Fig. 24), any dripping-induced shape failure or dimensional disruption was not observed, demonstrating process superiority of the PRISS cell as a new class of wearable power source. Here, to visualize

the unusual architecture of the PRISS cell, a transparent PDMS-coated PE film (thickness ~ 100 μm) was used as a flexible packaging material. Fig. 24 shows that the PRISS cell was directly fabricated on the paper-made eyeglasses and also operated a light emitting diode (LED) lamp connected to the power source-unitized, paper-made eyeglasses.

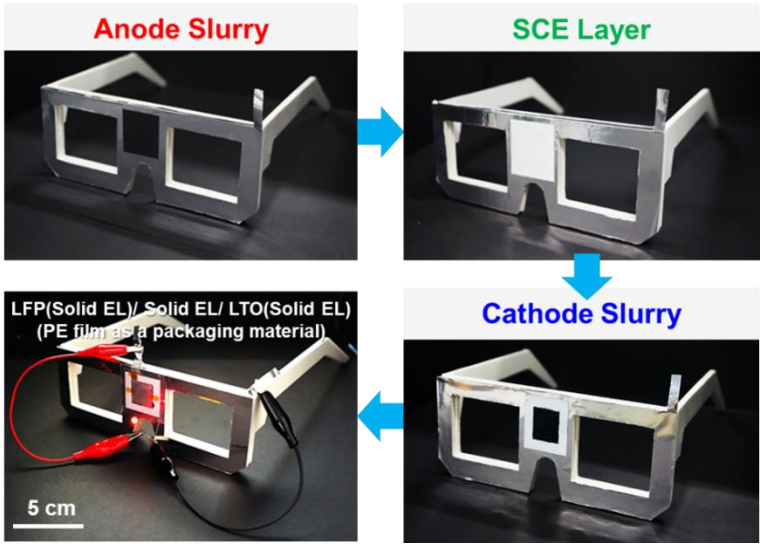

Fig. 24 A photograph showing direct fabrication of a PRISS cell on paper-made eyeglasses. The PRISS cell-unitized wearable eyeglasses operated a LED lamp.

To further highlight the versatile applicability and also shape-conformable feature of PRISS cells, a transparent glass cup was chosen as another example representing complex-shaped objects. Even on a curvilinear surface of the glass cup, a heart-shaped PRISS cell was fabricated using the aforementioned simple stencil printing and UV curing process. Fig. 25 exhibits that the PRISS cell, under being mounted on the round-shaped glass cup, delivers normal charge/discharge behavior.

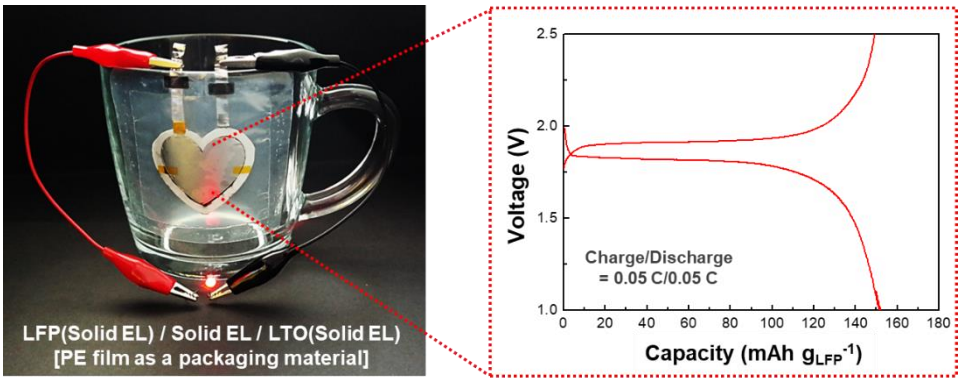

Fig. 25 A photograph showing direct fabrication of a heart-shaped PRISS cell on a transparent glass cup with curvilinear surface. The PRISS cell, under being mounted on the round-shaped glass cup, delivered normal charge/discharge behavior (at charge/discharge current density of 0.05 C/0.05 C under voltage range of 1.0 - 2.5 V, gravimetric charge/discharge capacity was estimated based on the mass of LFP active materials).

Notably, this unique printability of PRISS cells allows us to make letters-shaped power sources. Fig. 26 (left side) shows that the "PRISS" letters-shaped PRISS cell were successfully developed through the stencil printing and UV curing process. The letters-shaped PRISS cell presented normal charge/discharge profiles. Furthermore, to elucidate mechanical flexibility of the letters-shaped PRISS cell, the cells were completely wound along the rods having different diameters (= 5, 10, 15 mm), which ensured that the entire part of the cells was subjected to the same bending deformation. The charge/discharge behavior of the cells was examined under the fully wound state, not a planar configuration. The letters-shaped PRISS cell maintained its dimensional stability even after being mechanically bended and also showed no appreciable deterioration in the charge/discharge profiles.

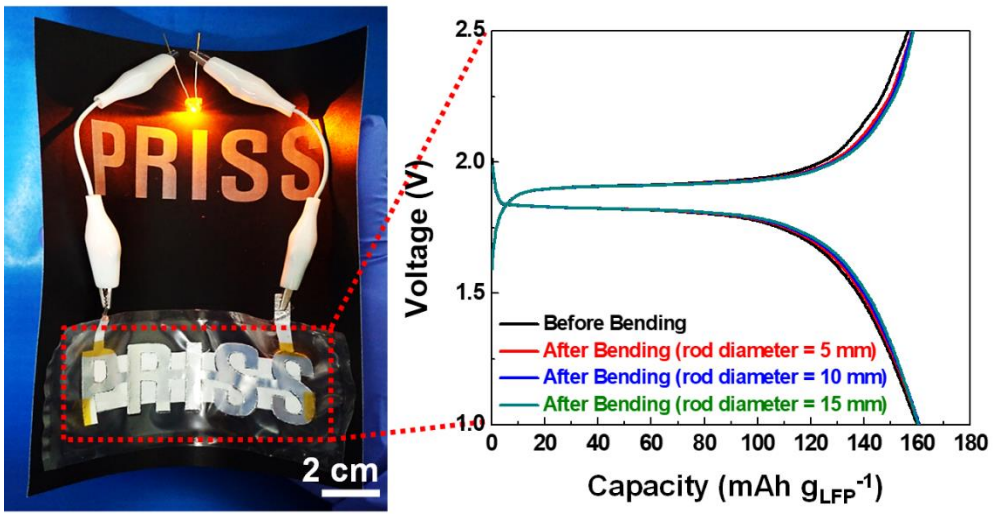

Fig. 26 A photograph of "PRISS" letters-shaped PRISS cell (left side) and its charge/discharge profiles at charge/discharge current density of 0.05 C/0.05 C under voltage range of 1.0 - 2.5 V (right side, gravimetric charge/discharge capacity was estimated based on the mass of LFP active materials), which were measured under being completely wound along the rods having different diameters (= 5, 10, 15 mm), not a planar configuration.

The abovementioned proof-of-concept results underscore the exceptional shape conformability/design universality/printability of PRISS batteries far beyond those accessible with conventional battery technologies. Future works will be devoted to improving electrochemical performance (including energy density, rate capability and long-term cycling performance) of PRISS cells, with a focus on the combination of new electrochemically-active materials[38-41] such as high-voltage/high-capacity electrode materials and high-conductive functional electrolytes.

3.1.4 Conclusion

In summary, we have presented the PRISS batteries as a versatile and scalable platform technology to open a new concept of cell architecture and fabrication route toward shape-conformable power sources with aesthetic versatility, which could overcome power source-related design/performance limitations in flexible/wearable electronic devices. The PRISS batteries were successfully fabricated through the simple stencil printing process followed by UV curing. The rheology control (toward thixotropic fluid behavior) of electrode slurries and SCE pastes, in combination with the well-tailored core elements including the UV-cured ETPTA polymer and high boiling point electrolyte, played key roles in realizing the exceptional printability. Such process and material uniqueness simplified the cell assembly process (specifically, being free from solvent drying/liquid-electrolyte injection/microporous separator membranes), thereupon enabling the fully-integrated multilayer-structured PRISS cells with various form factors far beyond those achievable by conventional battery technologies. More notably, the shape-conformable PRISS cells were seamlessly integrated with versatile-shaped objects such as paper-made eyeglasses and glass cups. In addition, the letters-shaped power sources were fabricated using the PRISS battery technology. The in-depth EIS analysis demonstrated the unique electrochemical characteristics of PRISS cells and also provided a theoretical basis to enable sustainable improvement of cell performance. We anticipate that the PRISS cells could be combined with fine-precision inkjet or three-dimensional printing techniques, which will offer unprecedented opportunities for development of multidimensional/multiscale complex-structured power sources. Future studies will be also focused on improving electrochemical performance of PRISS cells by introducing advanced electrochemically-active materials and optimizing their composition/architecture, along with continuing efforts toward making other cell components (for example, current collectors and packaging materials) printable, which will eventually enable direct fabrication of all-printable batteries with affordable and reliable electrochemical properties that are universally applicable to any arbitrary objects.

3.1.5 References

1. X. Lu; Y. Xia, Electonic materials: Buckling down for flexible electronics, Nanotechnol., 2006, 1, 163-164.
2. B. D. Gates, Flexible electronics, Science, 2009, 323, 1566-1567.
3. J. A. Rogers; T. Someya; Y. Huang, Materials and mechanics for stretchable electronics, Science, 2010, 327, 1603-1607.
4. M. J. Cima, Next-generation wearable electronics, Nat. Biotechnol., 2014, 32, 642-643.
5. J. Bae; M. K. Song; Y. J. Park; J. M. Kim; M. Liu; Z. L. Wang, Fiber supercapacitors made of nanowire-fiber hybrid structures for wearable/flexible energy storage, Angew. Chem. Int. Ed., 2011, 50, 1683-1687.
6. S. -Y. Lee; K. -H. Choi; W. -S. Choi; Y. -H. Kwon; H. -R. Jung; H. -C. Shin; J. -Y. Kim, Progress in flexible energy storage and conversion systems, with a focus on cable-type lithium-ion batteires, Energy Environ. Sci., 2013, 6, 2414-2423.
7. H. Gwon; J. Hong; H. Kim; D. -H. Seo; S. Jeon; K. Kang, Recent progress on flexible lithium rechargeable batteries, Energy Environ. Sci., 2014, 7, 538-551.
8. G. Zhou; F. Li; H. M. Cheng, Progress in flexible lithium batteries and future prospects, Energy Environ. Sci., 2014, 7, 1307-1338.
9. L. Li; Z. Wu; S. Yuan; X. B. Zhang, Advances and challenges for flexible energy storage and conversion devices and systems, Energy Environ. Sci., 2014, 7, 2101-2122.
10. X. Wang; X. Lu; B. Liu; D. Chen; Y. Tong; G. Sehn, Flexible energy-storage devices: Design consideration and recent progress, Adv. Mater., 2014, 26, 4763-4782.
11. Y. -H. Lee; J. -S. Km; J. Noh; I. Lee; H. J. Kim; S. Choi; J. Seo; S. Jeon; T. -S. Kim; J. -Y. Lee; J. W. Choi, Wearable textile battery rechargeable by solar energy, Nano Lett., 2013, 13, 5753-5761.
12. J. Ren; Y. Zhang; W. Bai; X. Chen; Z. Zhang; X. Fang; W. Weng;Y. Wang; H. Peng, Elastic and wearable wire-shaped lithium-ion battery with high electrochemical performance, Angew. Chem. Int. Ed., 2014, 53, 7864-7869.
13. K. -H. Choi; S. -J. Cho; S. -H. Kim; Y. H. Kwon; J. -Y. Kim; S. -Y. Lee, Thin, Deformable, and Safety-Reinforced Plastic Crystal Polymer Electrolytes for High-Performance Flexible Lithium-Ion Batteries, Adv. Funct. Mater., 2014, 24, 44-52.
14. L. Hu; M. Pasta; F. L. Mantia; L. Cui; S. Jeong; H. D. Deshazer; J. W. Choi; S. M. Han; Y. Cui, Stretchable, porous, and conductive energy textiles, Nano Lett., 2010, 10, 708-714.
15. L. Hu; H. Wu; F. La Mantia; Y. Yang; Y. Cui, Thin, flexible secondary Li-ion paper batteries, ACS Nano, 2010, 4, 5843-5848.
16. M. Kaempgen; C. K. Chan; J. Ma; Y. Cui; G. Gruner, Printable thin film supercapacitors

using single-walled carbon nanotubes, Nano Lett., 2009, 9, 1872-1876.

17. K. Jost; C. R. Perez; J. K. McDonough; V. Presser; M. Heon; G. Dion; Y. Gogotsi, Carbon coated textiles for flexible energy storage, Energy Environ. Sci., 2011, 4, 5060-5067.
18. W. Weng; Q. Sun; Y. Zhang; H. Lin; J. Ren; X. Lu; M. Wang; H. Peng, Winding aligned carbon nanotube composite yarns into coaxial fiber full batteries with high performances, Nano Lett., 2014, 14, 3432-3438.
19. H. -J. Ha; E. -H. Kil; Y. H. Kwon; J. Y. Kim; C. K. Lee; S. -Y. Lee, UV-curable semi-interpenetrating polymer network-integrated, highly bendable plastic crystal composite electrolytes for shape-conformable all-solid-state lithium ion batteries, Energy Environ. Sci., 2012, 5, 6491-6499.
20. S. -H. Kim; K. -H. Choi; S. -J. Cho; E. -H. Kil; S. -Y. Lee, Mechanically compliant and lithium dendrite growth-suppressing composite polymer electrolytes for flexible lithium-ion batteries, J. Mater. Chem. A, 2013, 1, 4949-4955.
21. Y. H. Kwon; S. -W. Woo; H. -R. Jung; H. -K. Yu; K. Kim; B. H. Oh; S. Ahn; S. -Y. Lee; S. -W. Song; J. Cho; H. -C. Shin; J. Y. Kim, Cable-type flexible lithium ion battery based on hollow multi-helix electrodes, Adv. Mater., 2012, 24, 5192-5197.
22. L. Kou; T. Huang; B. Zheng; Y. Han; X. Zhao; K. Gopalsamy; H. Sun; C. Gao, Coaxial wet-spun yarn supercapacitors for high-energy density and safe wearable electronics, Nat. Commun., 2014, 5, 3754-3767.
23. S. Xu; Y. Zhang; J. Cho; J. Lee; X. Huang; L. Jia; J. A. Fan; Y. Su; J. Su; H. Zhang; H. Cheng; B. Lu; C. Yu; C. Chuang; T. -I. Kim; T. Song; K. Shigeta; S. Kang; C. Dagdeviren; I. Petrov; P. V. Braun; Y. Huang; U. Paik; J. A. Rogers, Stretchable batteries with self-similar serpentine interconnects and integrated wireless recharging systems, Nat. Commun., 2013, 4, 1543-1550.
24. N. Singh; C. Galande; A. Miranda; A. Mathkar; W. Gao; A. L. M. Reddy; A. Vlad; P. M. Ajayan, Paintable battery, Sci. Rep., 2012, 2, 481-485.
25. Y. Xu; M. G. Schwab; A. J. Strudwick; I. Hennig; X. Feng; Z. Wu; K. Mullan, Screen-printable thin film supercapacitor device utilizing graphene/polyaniline inks, Adv. Energy Mater., 2013, 3, 1035-1040.
26. X. Wang; B. Liu; Q. Xiang; Q. Wang; X. Hou; D. Chen; G. Shen, Spray-Painted Binder-Free SnSe Electrodes for High-Performance Energy-Storage Devices, ChemSusChem, 2014, 7, 308-313.
27. K. Sun; T. -S. Wei; B. Y. Ahn; J. Y. Seo; S. J. Dillon; J. A. Lewis, 3D printing of interdigitated Li-Ion microbattery architectures, Adv. Mater., 2013, 25, 4537-4543.
28. W. J. Hyun; E. B. Secor; M. C. Hersam; C. D. Frisbie; L. F. Francis, High-resolution patterning of graphene by screen printing with a silicon stencil for highly flexible printed

electronics, Adv. Mater., 2015, 27, 109-115.

29. K. Hong; S. H. Kim; K. H. Lee; C. D Frisbie, Printed, sub-2V ZnO electrolyte gated transistors and inverters on plastic, Adv. Mater., 2013, 25, 3413-3418.
30. K. Fukuda; Y. Takeda; Y. Yoshimara; R. Shiwaku; L. T. Tran; T. Sekine; M. Mizukami; D. Kumaki; S. Tokito, Fully-printed high-performance organic thin-film transistors and circuitry on one-micron-thick polymer films, Nat. Commun., 2014, 5, 4147-4145.
31. K. -J. Baeg; N. Caironi; Y. -Y. Noh, Toward printed integrated circuits based on unipolar or ambipolar polymer semiconductors, Adv. Mater., 2013, 25, 4210-4244.
32. A. M. Gaikwad; G. L. Whiting; D. A. Steingart; A. C. Arias, Highly flexible, printed alkaline batteries based on mesh-embedded electrodes, Adv. Mater., 2011, 23, 3251-3255.
33. K. T. Braam; S. K. Volkman; V. Subramanian, Characterization and optimization of a printed, primary silver–zinc battery, J. Power Sources, 2012, 199, 367-372.
34. C. C. Ho; J. W. Evans; P. K. Wright, Direct write dispenser printing of a zinc microbattery with an ionic liquid gel electrolyte, J. Micromech. Microeng., 2010, 20, 104009-104017.
35. E. -H. Kil; K. -H. Choi; H. -J. Ha; S. Xu; J. A. Rogers; M. R. Kim; Y. -G. Lee; K. M. Kim; K. Y. Cho; S. -Y. Lee, Imprintable, bendable, and shape-conformable polymer electrolytes for versatile-shaped lithium-ion batteries, Adv. Mater., 2013, 25, 1395-1400.
36. F. Pignon; A. Magnin; J. -M. Piau, Thixotropic behavior of clay dispersions: combinations of scattering and rheometric techniques, J. Rheol., 1998, 42, 1349-1373.
37. J. E. Wallevik, Rheological properties of cement paste: thixotropic behavior and structural breakdown, Cem. Concr. Res., 2009, 39, 14-29.
38. K. Xu, Nonaqueous liquid electrolytes for lithium-based rechargeable batteries, Chem. Rev., 2004, 104, 4303-4417.
39. M. Armand; J. M. Tarascon, Building better batteries, Nature, 2008, 451, 652-657.
40. J. Hassoun; K. S. Lee; Y. K. Sun; B. Scrosati, An advanced lithium ion battery based on high performance electrode materials, J. Am. Chem. Soc., 2011, 133, 3139-3143.
41. V. Etacheri; R. Marom; R. Elazari; G. Salitra; D. Aurbach, Challenges in the development of advanced Li-ion batteries: a review, Energy Environ. Sci., 2011, 4, 3243-3262.

3.2 Flexible/Shape-Versatile, Bipolar All-Solid-State Lithium-Ion Batteries Prepared by Multistage Printing

3.2.1 Introduction

The forthcoming smart energy era, which will involve widespread use of flexible/wearable electronic devices, the Internet of Things (IoT), electric vehicles (EVs) and grid-scale energy storage systems (ESSs), has spurred the relentless pursuit of high-energy/safe rechargeable power sources.[1-3] In particular, recent fire/explosion accidents involving lithium-ion batteries (LIBs) has motivated researchers to devote greater attention to safety failures. As a promising solution to simultaneously address the aforementioned issues of energy density and safety, bipolar all-solid-state LIBs have attracted extensive attention.[4-9] The bipolar cell configuration enables minimal use of electrochemically inert components such as metallic foil current collectors and packaging substances, thereby contributing to a higher volumetric energy density beyond those achievable with a simple electrical connection of individual cells.

A key component in bipolar batteries is the solid-state electrolyte,[5,10] which acts as an ion-conducting separator membrane and as an electrolyte in bulk electrodes. To prevent the flow of ions between the adjacent cells (*i.e.*, to enable voltage build-up) inside bipolar batteries, nonfluidic solid-state electrolytes are essentially required. To date, (sulfide or oxide-based) inorganic solid electrolytes have been extensively investigated as attractive candidates;[4,6,11,12] however, their longstanding problems, which include poor ionic conductivity, high grain boundary resistance, mechanical brittleness, chemical/electrochemical instability and complicated synthetic processes, pose a formidable challenge to their practical application.

Several approaches have been undertaken to resolve the aforementioned issues of inorganic electrolytes, which include the synthesis of new inorganic electrolytes,[13-15] inorganic/polymer composite electrolytes[7-9,15-17] and porous nonwoven-reinforced inorganic electrolytes.11 Some meaningful progress has been reported in previous studies; however, many problems (particularly related to chemical/electrochemical stability, mechanical flexibility and form factors) still remain unresolved. In addition to these material challenges, the high-pressure/high-temperature sintering-based fabrication processes, which may not be suitable for continuous mass production, should also be resolved for their facile commercialization.

Here, we demonstrate a new class of flexible/shape-versatile bipolar all-solid-state LIBs as an unprecedented material/process strategy to address the aforementioned problems associated with inorganic-electrolyte-based bipolar LIBs. The new bipolar LIBs are easily fabricated via solvent-drying-free, ultraviolet (UV)-curing-assisted multistage printing. Instead of using conventional inorganic solid electrolytes, we develop a new flexible/nonflammable gel electrolyte (*i.e.*, sebaconitrile (SBN)-based electrolyte and a semi-interpenetrating polymer network (semi-IPN)

skeleton). The new gel electrolyte is incorporated as a core element into the printed electrodes and into the printed solid-state gel composite electrolytes (GCEs, functioning as an ion-conducting separator membrane). The flexible/nonflammable gel electrolyte eliminates concerns about grain boundary resistance (which is often encountered in inorganic-electrolyte-based cells) while also substantially improving the mechanical deformability, form factors, and thermal stability of the resultant printed electrodes and GCE. In addition, the gel electrolyte in the printed electrode acts as a binder that holds electrode active materials and carbon conductive additives, indicating no inclusion of conventional polymeric binders used in LIBs. The rheological properties of the printable electrode and GCE pastes are elaborately tailored to exhibit non-Newtonian fluid (specifically, thixotropic fluid) characteristics, thus enabling the realization of seamlessly integrated (in-series and in-plane) bipolar-stacked cells onto complex-shaped objects (*e.g.*, mini toy cars) via solvent-drying-free UV-assisted multistage printing. Notably, the multistage printing does not require the high-pressure/high-temperature sintering processes commonly used to fabricate inorganic-electrolyte-based bipolar all-solid-state LIBs.[5,13] We previously reported the advantageous effects (*i.e.*, short processing time, no use of processing solvents, no inclusion of conventional polymeric binders, no injection of liquid electrolytes) of the UV-curing-assisted printing process in cell fabrication elsewhere.[18,19] The rationally designed electrodes and GCEs, in conjunction with the multistage printing process, enable the facile fabrication of bipolar all-solid-state LIB cells with exceptional mechanical flexibility, form factors, stable charge/discharge behavior and nonflammability. A schematic of the flexible/shape-versatile bipolar cells prepared via the UV-assisted multistage printing process is shown in Fig. 27. Details on the cell fabrication are discussed in the following section.

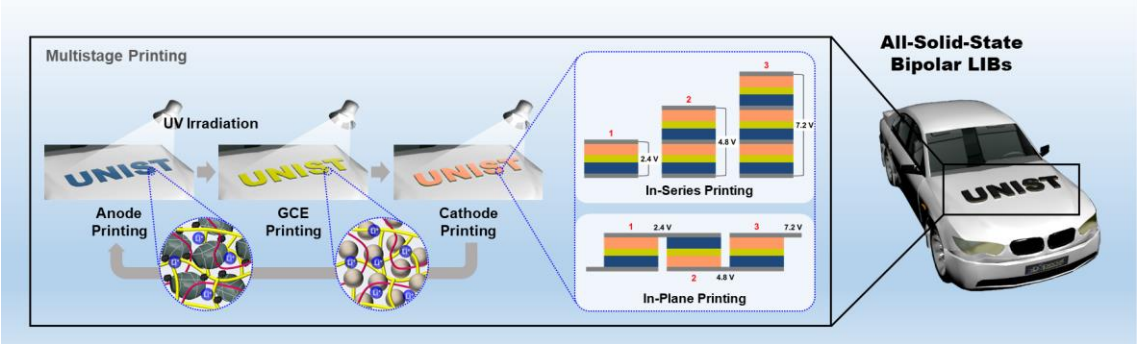

Fig. 27 Schematic illustration of the flexible/shape-versatile bipolar cells prepared via the UV-assisted multistage printing process.

3.2.2 Experimental

3.2.2.1 Preparation of the SWCNT-Coated Electrode Active Materials

The electrode active materials (here, $LiCoO_2$ (KD10, Umicore) and $LiTi_4O_{12}$ (Süd Chemie) powders were chosen for proof of concept) were added and mixed into single-walled carbon nanotubes (SWCNT) suspension. After being subjected to filtering followed by rinsing and drying, the SWCNT-coated electrode active powders were obtained.

3.2.2.2 Fabrication of the Printed Bipolar LIBs

To fabricate the printed electrodes, the as-prepared SWCNT-coated electrode powders were mixed with carbon black conductive additives and gel electrolyte precursors, thus yielding the electrode pastes. The composition ratios of the electrode pastes (electrode active powder/carbon black/gel electrolyte) were 55/6/39 (w/w/w) for the $LiCoO_2$ (LCO) cathode and 30/7/63 (w/w/w) for the $LiTi_5O_{12}$ (LTO) anode, respectively. Further optimization of the composition ratio will be implemented in our future studies. The gel electrolyte precursor was composed of the (1 M $LiBF_4$ in SBN) electrolyte and semi-IPN skeleton precursor (UV-curable ethoxylated trimethylolpropane triacrylate (ETPTA, Aldrich) incorporating 1.0 wt.% HMPP as a photoinitiator and poly(vinylidene fluoride-co-hexafluoropropylene) (PVdF-HFP) (Arkema, HFP content = 6 mol%), ETPTA/PVdF-HFP = 75/25 (w/w)). The composition ratio of the (1 M $LiBF_4$ in SBN) electrolyte and semi-IPN skeleton precursor was 85/15 (w/w). The LTO anode paste was printed on an Al current collector using a stencil printing technique without any processing solvents and was then exposed to UV irradiation, resulting in the printed LTO anode. UV irradiation was performed using an Hg UV-lamp (Lichtzen) with an irradiation peak intensity of approximately 2000 mW cm^{-2}. Subsequently, on top of the LTO anode, the GCE paste (gel electrolyte precursor/Al_2O_3 nanoparticles (average particle size ~300 nm) = 60/40 (w/w)) was introduced *via* the same stencil printing and UV curing process, leading to a printed solid-state GCE layer on the LTO anode. The printed LCO cathode was then fabricated by printing the LCO cathode paste directly onto the GCE layer/LTO anode unit, followed by UV irradiation. After the Al current collector was placed on top of the printed LCO cathode/printed GCE layer/printed LTO anode assembly, a seamlessly integrated all-solid-state mono full cell was obtained. On top of the as-prepared mono full cell, the printing/UV curing processes were repeatedly conducted, enabling the fabrication of the printed bipolar cells (with in-series or in-plane configuration). Note that the LTO anode and LCO cathode shared the Al foil as a common current collector.

3.2.2.3 Structural/Rheological/Physical Characterization of the Printed GCE and Electrodes

The UV curing reaction of the printed GCE and electrodes was examined using an FT-IR spectrometer (Alpha Platinum ATR, Bruker) with a spectral resolution of 4 cm^{-1}. The glass transition temperatures (T_{gs}) of the semi-IPN were examined by differential scanning calorimetry (Q200, TA Instruments, heating rate = 10 °C min^{-1}). The weight loss of the printed GCE and electrodes was estimated as a function of temperature using a thermogravimetric analyzer (Q500, TA Instruments, heating rate = 10 °C min^{-1}) with the sample under a nitrogen atmosphere. The ionic conductivity of the printed GCE was measured with an impedance analyzer (VSP classic, Bio-Logic) over a frequency range from 1 to 10^6 Hz. The electronic conductivities of the printed electrodes were estimated using a four-point probe technique (CMTSR1000N, Advanced Instrument Technology). The interfacial exothermic reaction between the delithiated LCO and the electrolyte was measured by differential scanning calorimetry (Q200, TA Instruments, heating rate = 10 °C min^{-1}). The morphologies of the printed GCE and electrodes were characterized using field-emission scanning electron microscopy equipped with energy-dispersive X-ray spectroscopy (S4800, Hitachi). The mechanical flexibility of the printed GCE and electrodes was investigated under various deformation modes such as bending and folding. The rheological properties of the printable GCE and electrode pastes were investigated using a rheometer (Haake MARS 3, Thermo Electron GmbH).

3.2.2.4 Fabrication and Electrochemical Performance of the Printed Bipolar LIBs

The printed LIBs were fabricated using 2032-type coin cells (for half cells) and Al pouch cells (for mono and bipolar-stacked full cells, width and length of 10 mm × 10 mm). The assembly of the cells was performed in an argon-filled glove box. A control cell was prepared by assembling an LCO cathode, LTO anode and polyethylene (PE) separator (thickness = 20 ㎛, Tonen), followed by filling with the carbonate-based liquid electrolyte (1 M $LiPF_6$ in EC/DMC = 1/1 v/v). The electrochemical performance of the cells was investigated under various charge/discharge conditions using a cycle tester (PNE Solution).

3.2.3 Results and Discussion

3.2.3.1 Synthesis and Characterization of the Printed GCE

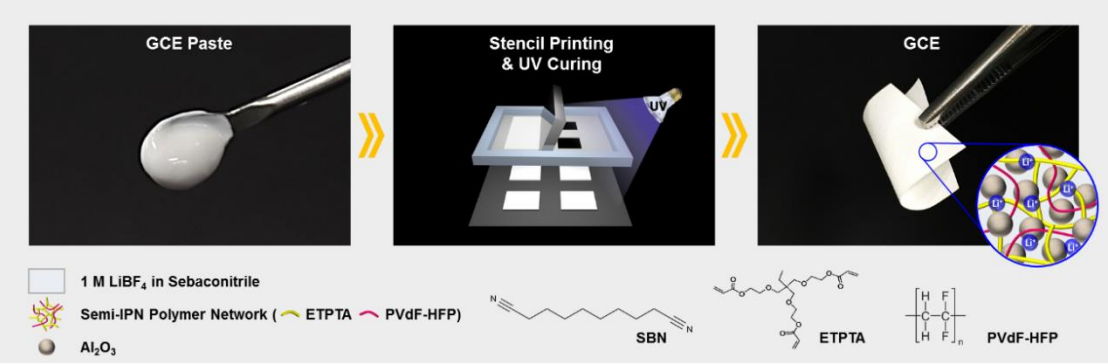

Fig. 28 Schematic of the procedure used to fabricate the stencil-printed GCE, along with photographs of the GCE and chemical structure of its major components. The GCE consisted of the gel electrolyte ((1 M $LiBF_4$ in SBN) electrolyte and semi-IPN skeleton) and Al_2O_3 nanoparticles.

The fabrication procedure of the printed GCE, along with its photographs and chemical structure of the major components, is depicted in Fig. 28. The GCE pastes (*i.e.*, prior to UV curing) were stencil-printed onto a substrate and then solidified upon exposure to UV irradiation for a short time (< 30 s) without using any processing solvents.

The solid-state GCE was composed of the gel electrolyte (1 M $LiBF_4$ in SBN/semi-IPN skeleton = 85/15 (w/w))) and Al_2O_3 nanoparticles (average particle size ≈ 300 nm), wherein the composition ratio of the gel electrolyte/Al_2O_3 nanoparticles was 60/40 (w/w). The Al_2O_3 nanoparticles were incorporated as a mechanical spacer to prevent electrical contact between the electrodes and as a rheology-tuning agent for the printing process.[18,19] The composition ratio of gel electrolyte/Al_2O_3 nanoparticles = 60/40 (w/w) was determined by considering both rheological behavior (related to printing processability) of the GCE pastes and ionic conductivity of the resulting GCE films (Fig. 29). The SBN, because of its superb thermal stability and reliable electrochemical performance,[20-22] was chosen as a new Li-ion-conducting medium that outperforms conventional carbonate-based ones.

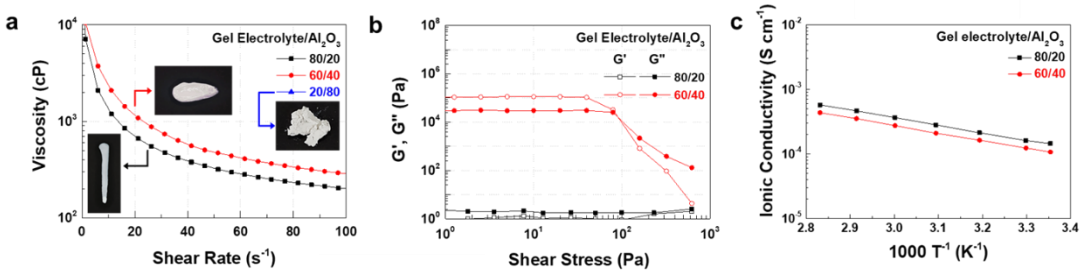

Fig. 29 Rheological properties and ionic conductivity of the GCE pastes as a function of the ratio of gel electrolyte/Al2O3 nanoparticles. (a) Shear rate-dependent viscosity and photographs (inset images). The GCE paste (gel electrolyte/Al2O3 = 20/80) failed to measure its rheological properties due to serious particle agglomeration. (b) Viscoelastic properties (G' and G") of the GCE pastes as a function of shear stress. (c) Ionic conductivity of the printed GCE films as a function of temperature.

Cross-sectional SEM and EDS images of the resulting GCE film show that the Al_2O_3 nanoparticles were uniformly and compactly dispersed in the through-thickness direction (Fig. 30). In addition, highly percolated interstitial voids formed between the Al_2O_3 nanoparticles were observed in the GCE film; these voids were originally occupied by the SBN-based electrolyte that was etched using dimethyl carbonate prior to the SEM analysis.

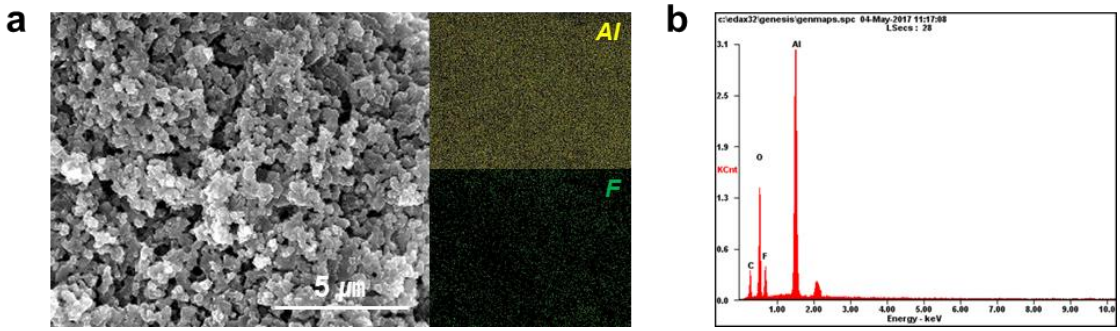

Fig. 30 (a) Cross-sectional SEM and EDS images showing the dispersion state of Al2O3 nanoparticles and the presence of interstitial voids (originally occupied by the SBN-based electrolyte) in the printed GCE. (b) EDS mapping area of Al and F elements in the printed GCE

Another important component of the GCE film is the semi-IPN skeleton, which consists of a UV-crosslinked ETPTA network and PVdF-HFP, wherein the composition ratio of ETPTA/PVdF-HFP is 75/25 (w/w). We previously reported[23] that the semi-IPN skeleton in gel polymer electrolytes effectively improves both their mechanical flexibility and their ionic conductivity. The (ETPTA/PVdF-HFP) semi-IPN structure was characterized by measuring the T_{gs} of the ETPTA polymer network and the PVdF-HFP (Fig. 31a). Two different T_{gs} (71 °C for the UV-cured ETPTA polymer network and -24 °C for the PVdF-HFP), which are similar to those of the pristine ETPTA network and PVdF-HFP (insets of Fig. 31a), were observed for the semi-IPN, indicating phase separation of the ETPTA network and the PVdF-HFP. To confirm this phase-separated structure, a semi-IPN film without Al_2O_3 nanoparticles was prepared as a model system, and its SEM image was analyzed after selective removal of the PVdF-HFP. A large number of pores originating from the PVdF-HFP were uniformly dispersed in the ETPTA matrix (Fig. 31b), verifying the well-developed phase separation between the ETPTA matrix and PVdF-HFP in the semi-IPN. In addition, the photocuring of the ETPTA matrix was verified by observing the change in the FT-IR peaks (Fig. 31c) assigned to the acrylic C=C bonds (1610–1625 cm^{-1}) of the ETPTA and the insoluble polymer fraction (> 99%)[19,24] after exposure to UV irradiation. The semi-IPN skeleton plays a viable role in the mechanical flexibility of the GCE film (Fig. 31d). No structural disruption was observed in the GCE film even after 10,000 bending cycles (bending radius = 5 mm, deformation rate = 10 mm min^{-1}).

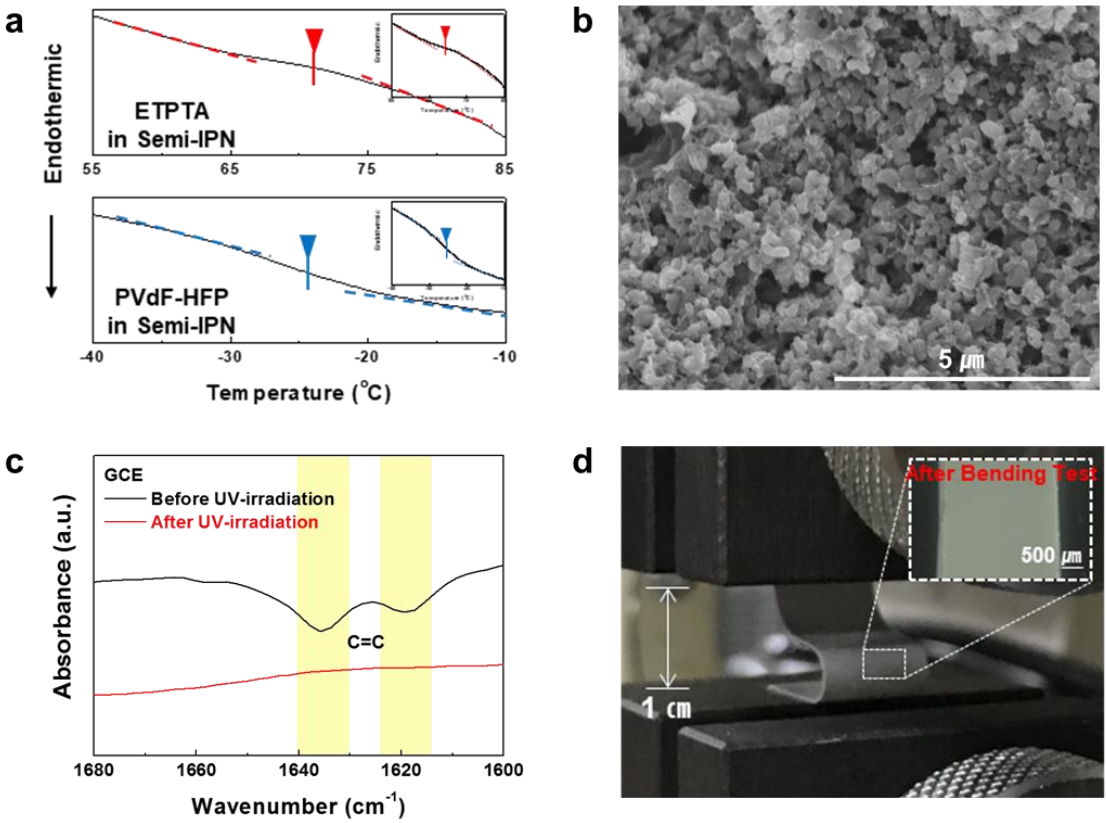

Fig. 31 Mechanical properties of GCE, (a) DSC thermograms showing two different T_{gs} of the ETPTA polymer network and PVdF-HFP in the semi-IPN. The insets show the (T_{gs}) of the pristine ETPTA polymer network and PVdF-HFP, respectively, (b) SEM morphology of the (ETPTA/PVdF-HFP = 75/25 (w/w)) semi-IPN film; the PVdF-HFP was selectively etched prior to the SEM analysis, (c) Change in the characteristic FT-IR peaks assigned to the acrylic C=C bonds (1610–1625 cm^{-1}) of the ETPTA in the printed GCE before/after UV irradiation, (d) The mechanical flexibility of the printed GCE upon the bending cycles (bending radius = 5 mm, deformation rate = 10 mm min^{-1}).

The ionic conductivity of the GCE was measured as a function of temperature (Fig. 32a). Over a wide range of temperature, the GCE delivered satisfactory ionic conductivity, demonstrating the formation of well-developed ion channels. A salient feature of the GCE is its thermal stability. The thermogravimetric analysis (TGA) profiles (Fig. 32b) show that the GCE is negligibly volatile until 150 °C because of the high boiling point (200 °C) of SBN, whereas a conventional carbonate-based liquid electrolyte (1 M $LiPF_6$ in EC/DMC = 1/1 (v/v)) exhibited substantial weight loss even below 100 °C. To further verify this superior thermal stability, the isothermal ionic conductivity of the GCE was compared with that of the carbonate-based electrolyte at a high temperature (80 °C). The GCE exhibited stable ionic conductivity for longer than 100 h, whereas the carbonate-based electrolyte rapidly lost ionic conductivity after 30 h (Fig. 32c). In addition, the GCE exhibits nonflammable behavior (Fig. 32d), unlike the flammable carbonate-based electrolyte. This nonflammability of the GCE demonstrates its promising potential as a new alternative to inorganic solid electrolytes in terms of battery safety.

The GCE described above was compared with the previously reported sulfide (or oxide)-based electrolytes in order to underline its unique characteristics, with special attention to synthesis, ionic conductivity, thickness as a separator membrane, mechanical flexibility, safety and shape versatility.

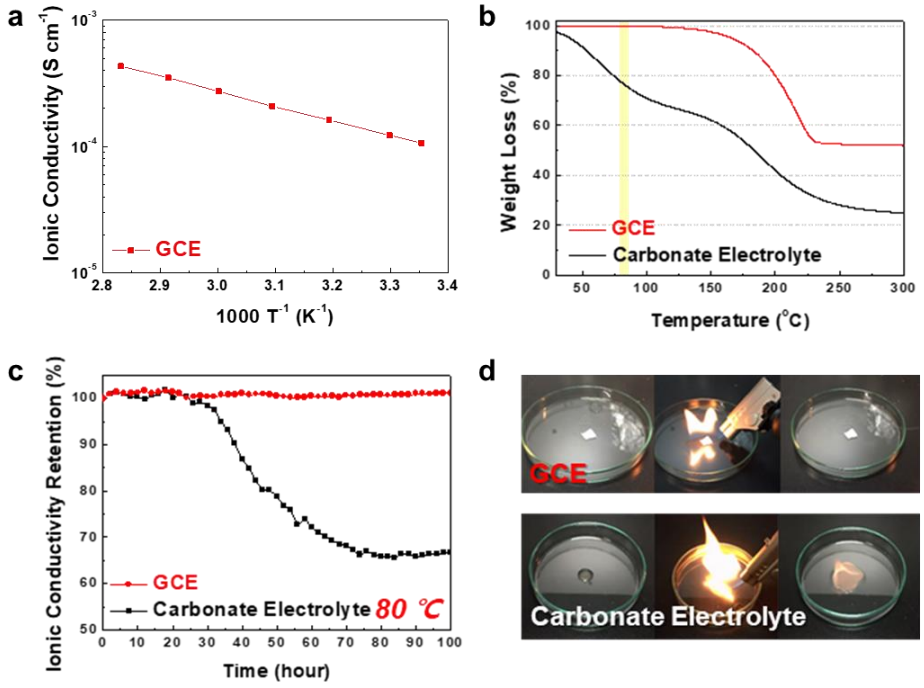

Fig. 32 (a) The ionic conductivity of the printed GCE as a function of temperature. (b) TGA profiles of the GCE and carbonate-based control electrolyte (1 M LiPF6 in EC/DMC = 1/1 (v/v)) chosen as the control electrolyte. (c) The isothermal (80 ºC) ionic conductivity of the GCE and carbonate-based control electrolyte as a function of time. (d) The nonflammability test of the GCE (top photographs) and the carbonate-based control electrolyte (bottom photographs).

3.2.3.3 Fabrication and Characterization of the Printed Electrodes

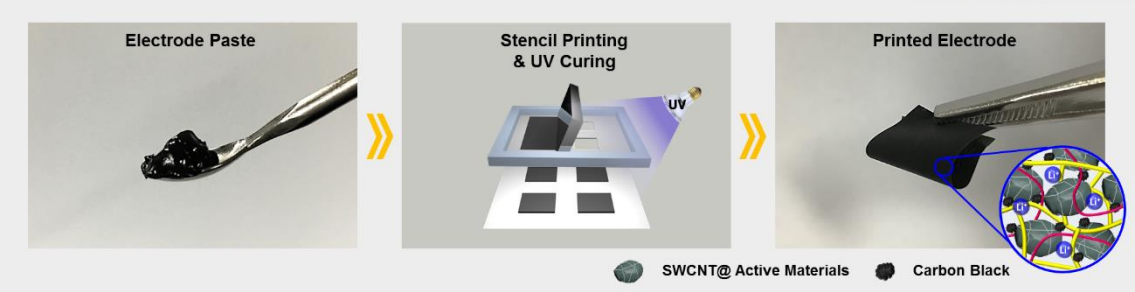

Fig. 33 Schematic of the procedure used to fabricate the stencil-printed electrode, along with photographs of the electrode. The printed electrodes consisted of the gel electrolyte ((1 M $LiBF_4$ in SBN) electrolyte and semi-IPN skeleton), carbon black additive and an electrode active material (LCO and LTO powders were chosen for proof of concept).

The printed electrodes consisted of the gel electrolyte (1 M $LiBF_4$ in SBN/semi-IPN skeleton), carbon black conductive additives and electrode active materials. Here, as a proof-of-concept, LCO and LTO powders were chosen for the printed cathodes and anodes, respectively. The fabrication procedure of the printed electrode, along with its photograph and major components, are schematically depicted in Fig. 33. The formation of the UV-cured ETPTA polymer network in the semi-IPN skeleton of the printed electrodes was verified by the changes in the FT-IR peaks assigned to the acrylic C=C bonds (Fig. 34). The composition ratios of the printed electrodes were electrode active powder/carbon black additive/gel electrolyte = 55/6/39 (w/w/w) for the LCO cathode and 30/7/63 (w/w/w) for the LTO anode. Note that the printed electrodes already included the gel electrolyte as a major element, indicating that no additional incorporation of electrolytes into the electrodes was needed. This result was similar to those of previously reported inorganic-electrolyte-embedded bulk electrodes.[25,26] In addition to this role as an ion conductor, the gel electrolyte in the printed electrode also acted as a binder that holds electrode active materials and carbon black additives, revealing that traditional polymeric binders such as polyvinylidene fluoride (PVdF) and carboxymethyl cellulose (CMC)/styrene-butadiene rubber (SBR) were not included. Fig. 35 shows that the LCO powders and carbon black additives are uniformly dispersed in the through-thickness direction of the printed LCO cathode. In addition, highly reticulated interstitial voids (originally occupied by the SBN-based gel electrolytes) were formed between the powders.

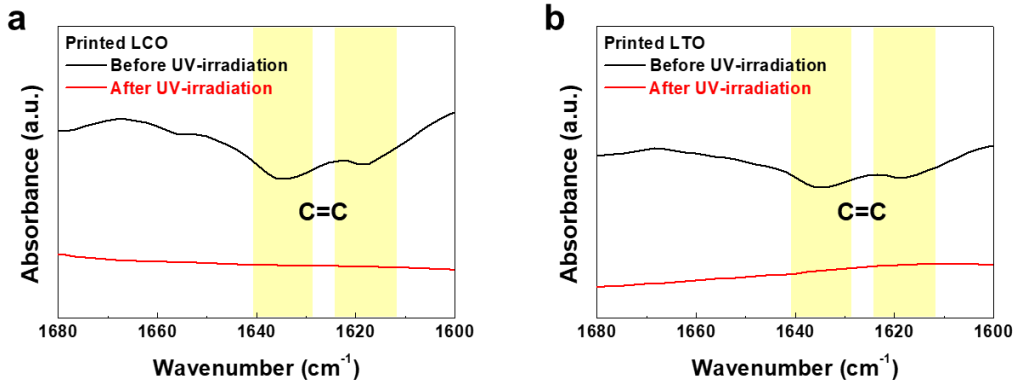

Fig. 34 Change in the characteristic FT-IR peaks assigned to the acrylic C=C bonds (1610–1625 cm^{-1}) of the ETPTA before/after UV irradiation: (a) printed LCO cathode and (b) printed LTO anode.

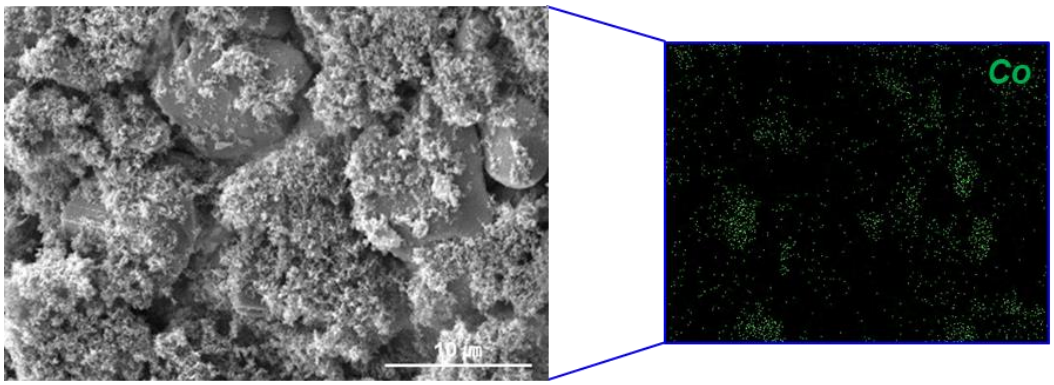

Fig. 34 Cross-sectional SEM and EDS images showing the dispersion state of the LCO powders and the presence of interstitial voids (originally occupied by the SBN-based electrolyte) in the printed LCO cathode. (c) SEM image of the SWCNT-coated LCO powders. The inset shows the morphology of the pristine LCO powders.

Prior to fabricating the printed electrodes, the LCO and LTO powders were coated with SWCNTs to improve their electronic conductivity. Similar approaches based on CNT-mediated surface modification have been reported in previous publications.[27-29] Details of the coating procedure are described in the experimental section. Fig. 36a shows that the LCO particles were coated with highly reticulated SWCNT networks. The solid content in the LCO/SWCNT suspension solution was 4.6 wt%. From the TGA profiles (Fig. 36b, c), the compositional ratios of the SWCNT-coated electrode active powders were estimated to be LCO/SWCNT = 99.75/0.25 (w/w) and LTO/SWCNT = 99.35/0.65 (w/w), respectively. The introduction of the electrically conductive SWCNT layers on the LCO (and LTO) surface led to an increase in the electronic conductivity of the resulting electrodes (Fig. 36d, e). As a consequence, the SWCNT-coated LCO showed remarkable improvement in discharge rate capability (Fig. 36f), where coin-type half cells (Li metal anode/PE separator/LCO cathode) were examined at a constant charging current density of 0.1 C.

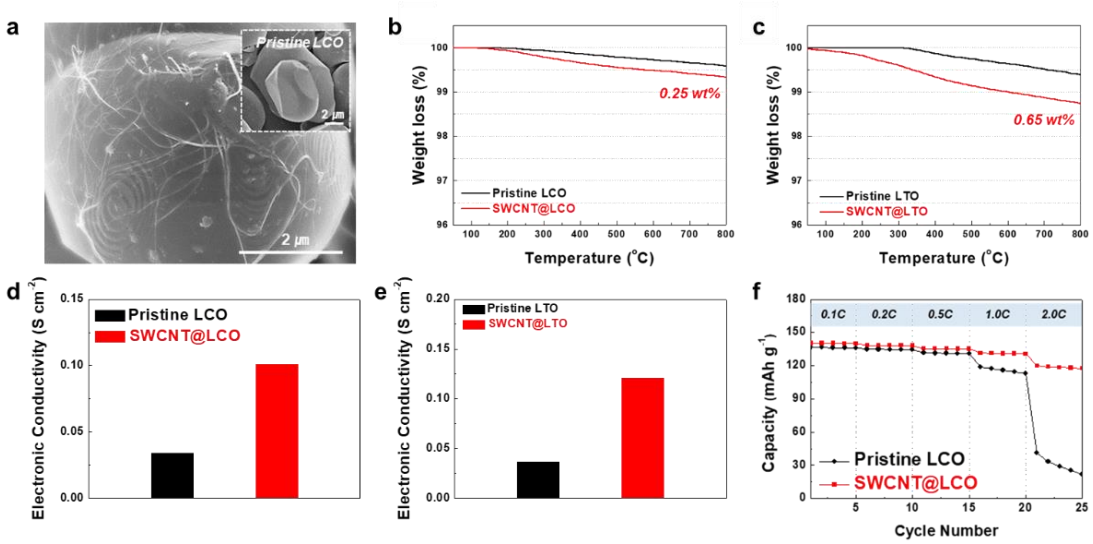

Fig. 35 (a) SEM image of the SWCNT-coated LCO powders. The inset shows the morphology of the pristine LCO powders. TGA profiles of the SWCNT-coated electrode active powders, (b) SWCNT-coated LCO, (c) SWCNT-coated LTO. Comparison of the electronic conductivity, (d) SWCNT-coated LCO and pristine LCO, (e) SWCNT-coated LTO and pristine LTO. (f) Comparison of the discharge rate capability between the SWCNT-coated LCO and pristine LCO, where coin-type half cells (Li metal anode/PE separator/LCO cathode) were examined at a constant charge current density of 0.1C.

To quantitatively analyze the mechanical flexibility of the electrodes, their electronic resistance was monitored as a function of the longitudinal compression cycle (bending radius = 5 mm, deformation rate = 10 mm min^{-1}). The printed LCO cathode showed no substantial change in electronic resistance after 600 bending cycles (Fig. 37a). By contrast, the electronic resistance of the control LCO cathode (prepared by slurry casting, LCO/carbon black/PVdF binder = 95/2/3 (w/w/w)) fluctuated with the bending cycle and eventually mechanically broke after 66 cycles. To further visualize this superior flexibility, the printed LCO cathode was subjected to multi-folding (Fig. 37b). Neither detectable cracks nor defects were observed at the printed LCO cathode, whereas the control LCO cathode showed structural rupture at the folded edges. These results demonstrate that the semi-IPN skeleton plays an important role in the enhancement of the mechanical flexibility of the printed LCO cathode.

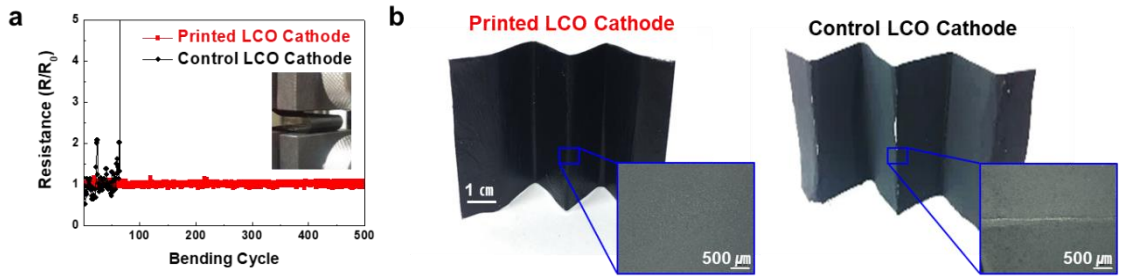

Fig. 36 (a) Change in the electronic resistance of the printed LCO cathode (vs. control LCO cathode (LCO/carbon black/PVdF binder = 95/2/3 (w/w/w)) prepared by slurry casting) as a function of the longitudinal compression cycle (bending radius = 5mm, deformation rate = 10mm min^{-1}).
(b) Photographs showing the multi-folding of the printed LCO and control LCO cathodes.

The thermal stability of the printed electrodes was investigated. Fig. 38a compares the TGA profiles of the printed LCO cathode (the SBN/semi-IPN gel electrolyte was already included) and the control LCO cathode incorporating the carbonate-based liquid electrolyte (1 M $LiPF_6$ in EC/DMC = 1/1 (v/v)). Negligible weight loss was observed at the printed LCO cathode up to 150 °C, whereas the control LCO cathode showed rapid weight loss due to volatilization of the carbonate liquid electrolyte. In addition, the interfacial exothermic reaction between the delithiated LCO materials and electrolytes was examined (Fig. 38b). The thermogram of the control LCO cathode shows two characteristic exothermic peaks (Tpeak = 220 and 250 °C), indicating vigorous interfacial exothermic reactions.[30, 31] By contrast, the exothermic peaks were shifted to higher temperatures in the printed LCO cathode. To highlight this superb thermal stability of the printed LCO cathode, a flammability test of the delithiated LCO cathode was conducted. The printed LCO cathode showed no flame even upon exposure to an ignition lighter, whereas the control LCO cathode instantly caught fire (Fig. 38c). The aforementioned results

demonstrate that the (SBN/semi-IPN) gel-electrolyte-embedded printed electrodes could be used to prevent fire or explosion accidents in LIBs.

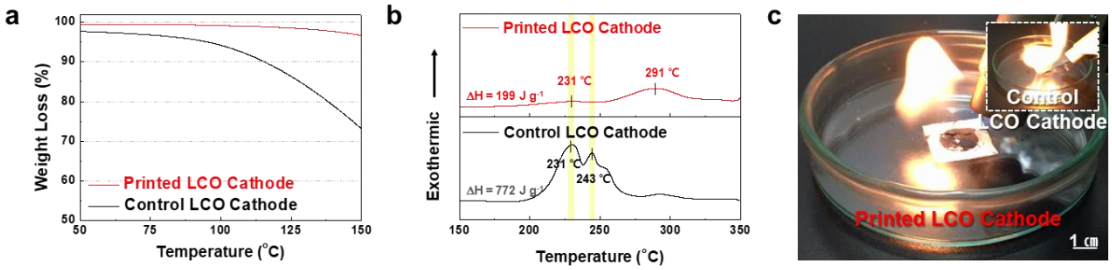

Fig. 37 Comparison of the thermal stability of the printed LCO and control LCO cathodes incorporating the carbonate-based liquid electrolyte (1 M $LiPF_6$ in EC/DMC = 1/1 (v/v)): (a) TGA profiles; (b) DSC thermograms showing interfacial exothermic reactions between delithiated LCO and electrolytes; (c) nonflammability tests of the printed LCO cathode (left photograph) and the control LCO cathode (right photograph).

3.2.3.4 Rheology Control of the GCE and Electrode Pastes for Multistage Printing

Compared with the sintering processes commonly used to prepare inorganic-electrolyte-based bipolar all-solid-state LIBs, UV-curing-assisted printing provides a noteworthy advantage of eliminating the need for high-pressure/high-temperature sintering, thus enabling the facile fabrication of bipolar LIBs with various form factors. A prerequisite for the printing process is control of the rheological properties of the printable GCE and electrode pastes. A basic understanding of the relationship between the rheological properties of the electrode/electrolyte pastes and the printing processability was reported in our previous studies.[18, 19, 32]

Fig. 39a shows that the viscosities of the GCE and electrode pastes tend to decrease with increasing shear rate, revealing their shear-thinning behaviors. The viscoelasticity analysis (Fig. 39b) reveals that the storage modulus (G′) is higher than the loss modulus (G″) in the low-shear-stress region and that the opposite trend occurs in the high-shear-stress region, thereby demonstrating typical thixotropic fluid behavior[19, 33] that is suitable for the stencil printing process. Such thixotropic fluid behavior was further verified by the hysteresis loops[34] in the rheograms (*i.e.*, flow curves) (Fig. 39c). These well-tuned rheological properties enabled the realization of a (letter-shaped) printed GCE and LCO cathode on miniature toy cars with curvilinear surfaces (Fig. 39d).

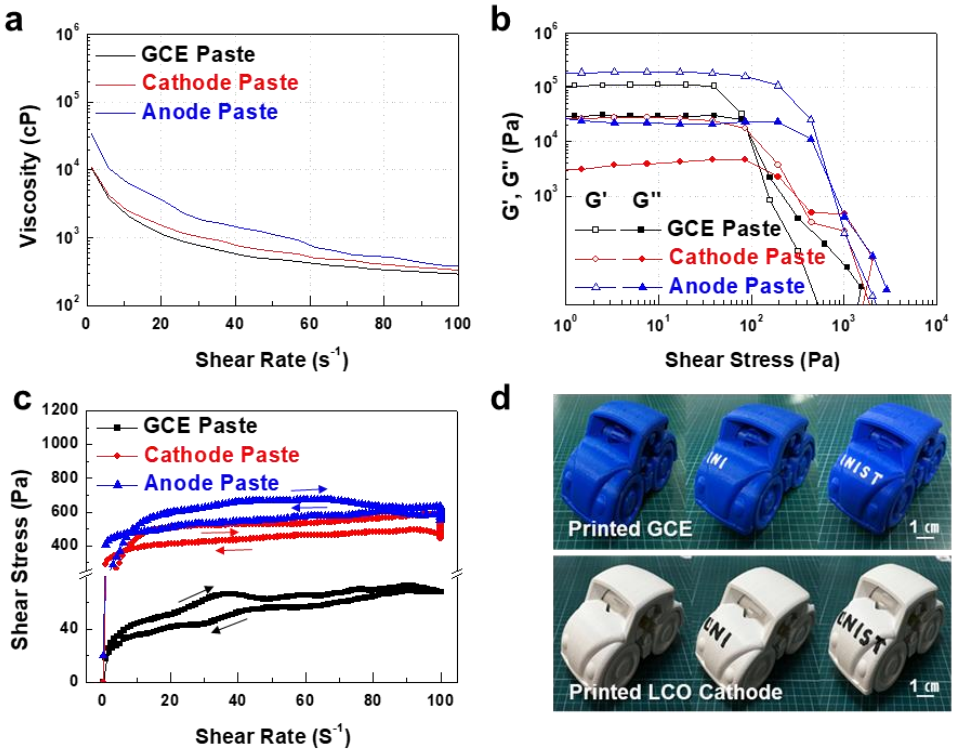

Fig. 38 (a) Viscosities of the GCE and electrode pastes as a function of shear rate. (b) Viscoelastic properties (G' and G") as a function of shear stress. (c) Hysteresis loops in the rheograms. (d) Photographs showing the fabrication of the (letter-shaped) printed GCE (top photographs) and LCO cathode (bottom photographs) on miniature toy cars with curvilinear surfaces.

On the basis of our understanding of the above-described physicochemical/rheological characteristics of the GCE and electrode pastes, we fabricated bipolar-stacked LIBs through stencil-based multistage printing followed by UV curing. As depicted in the Fig. 27, the LTO anode, GCE and LCO cathode pastes were sequentially stencil-printed onto Al foil current collectors and then solidified by UV curing, yielding a printed mono full cell. In the printed mono full cell, the LTO anode, GCE layer and LCO cathode were seamlessly integrated. On top of the as-prepared mono full cell, the UV-curing-assisted printing process was repeatedly conducted, eventually leading to the fabrication of bipolar-stacked cells. Here, the LTO anode and LCO cathode shared the Al foil as a common current collector. Fig. 40a shows a cross-sectional SEM image of the printed bipolar 3-stacked cells in which the three cells were connected in series. Neither delamination nor cracking was observed between the mono full cells in the bipolar 3-stacked cells.

Another advantage of the multistage printing process is the facile realization of printed bipolar cells with an in-plane configuration. On top of an Al foil current collector, the LCO cathode and LTO anode pastes were printed side-by-side and subjected to UV curing. Subsequently, the GCE pastes were printed/UV-cured onto the as-prepared LCO cathode and LTO anode. The electrode pastes were then again printed side-by-side onto the GCE layers and UV-cured. After an Al foil current collector was placed on top of the final electrode layers, the fabrication of the bipolar-stacked cells with in-plane configuration were completed. This stepwise fabrication process, along with the corresponding photographs, is illustrated in Fig. 40b. We again emphasize that processing solvents (and solvent drying steps), porous separator membranes and liquid-electrolyte injection were not needed in the UV-assisted multi-stage printing, underscoring the simplicity and scalability of the process presented herein.

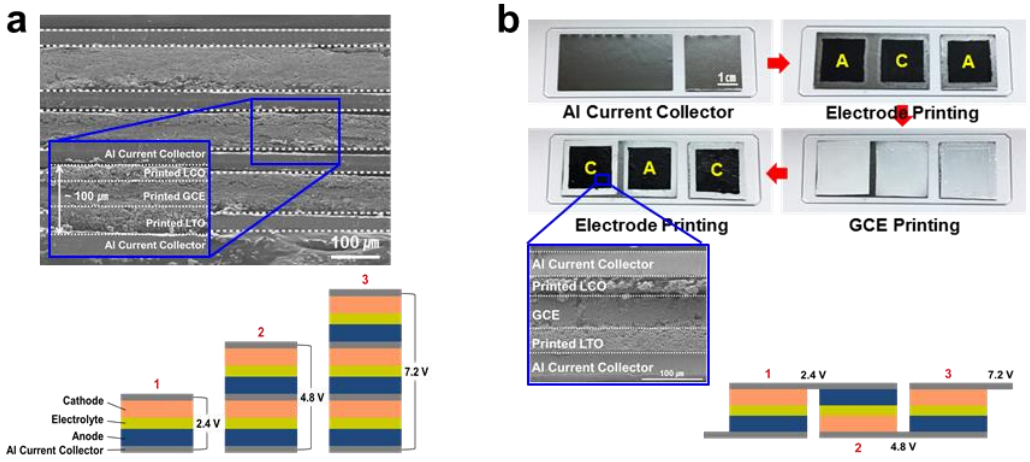

Fig. 39 (a) Cross-sectional SEM image of the printed bipolar cells (here, the three cells were connected in series) and schematic of their structures, wherein the LTO anode and LCO cathode shared the Al foil as a common current collector. (f) Cross-sectional SEM image of the printed bipolar cells (here, the three cells were connected in parallel) and schematic of their structures.

3.2.3.5 Electrochemical Characterization of the Printed Bipolar Cells

The electrochemical performance of the printed bipolar cells was characterized at room temperature. As a first step, the charge/discharge behaviors of the printed LCO cathode and LTO anode were investigated, wherein a coin-type half cell (printed LCO cathode (or printed LTO anode)/(1 M $LiBF_4$ in SBN)-soaked PE separator/lithium metal) was cycled at a fixed charge/discharge current density of 0.1 C/0.1 C in the voltage ranges from 3.0 to 4.2 V and from 1.0 to 2.5 V, respectively. Fig. 41a shows that the printed LCO cathode and LTO anode presented the stable charge/discharge profiles during cycling. Next, the printed mono full cell (LCO cathode/GCE/LTO anode, Al pouch-type cell) was cycled between 1.5 and 2.7 V at a constant charge/discharge current density (0.05 C/0.05 C). The mono full cell showed normal charge/discharge behaviour without any internal short-circuit failure and also reasonable capacity retention (= 95 % after the 50th cycle) during cycling (Fig. 41b). In addition, no structural disruption in the cell was observed after the cycle test (Fig. 41d). These results demonstrate the electrochemical viability of the printed full cell as a new solid-state LIB.

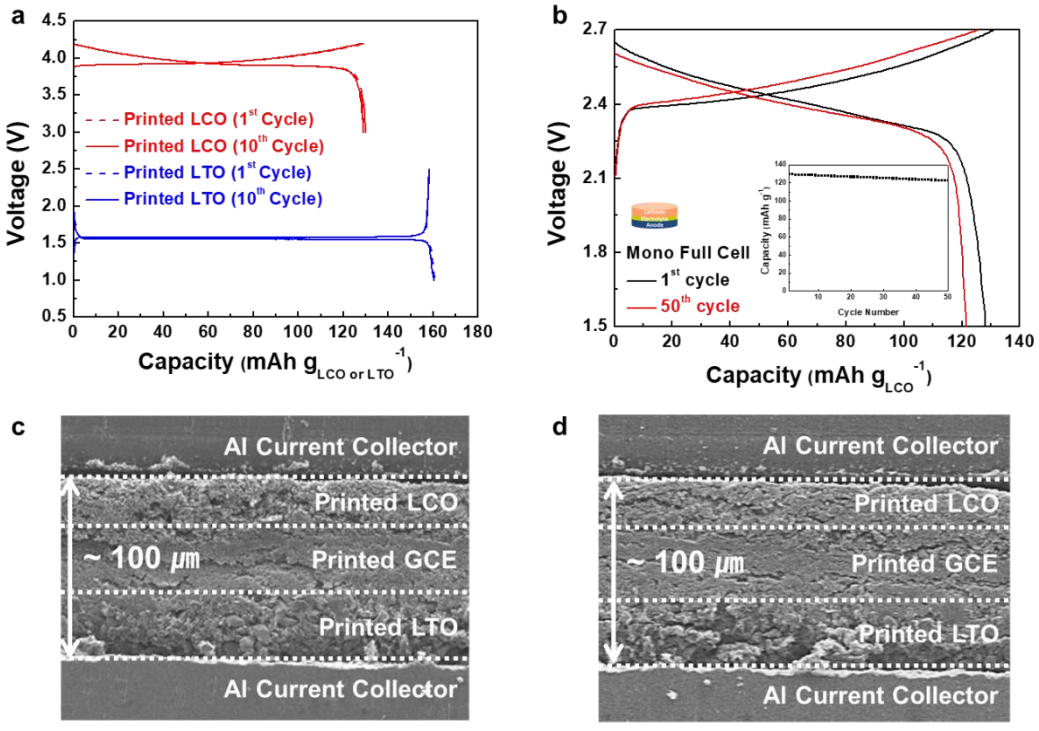

Fig. 40 (a) Charge–discharge profiles of the printed LCO cathode and LTO anode, where a coin-type half cell (printed LCO cathode (or printed LTO anode)/(1 M $LiBF_4$ in SBN)-soaked PE separator/lithium metal) was cycled at a fixed charge/discharge current density of 0.1C/0.1C in the voltage range from 3.0 to 4.2 V and from 1.0 to 2.5 V, respectively. (b) Cycling performance of the printed mono full cell (LCO cathode/GCE/LTO anode), where the cell was cycled between 1.5 and 2.7 V at a constant charge/discharge current density (0.05C/0.05C). Cross-sectional SEM image of the printed mono full cell (composed of an LTO anode, GCE layer and LCO cathode). (c) Before the cycle test. (d) After the 50th cycle.

The charge/discharge profiles of the printed bipolar cells with an in-series configuration were compared as a function of cell number (Fig. 42a). As the cell number increased, the working voltages of the resulting cells increased from 2.4 V (mono cell) to 5.4 V (two cells) to 7.2 V (three cells). The cycling stability of the printed bipolar cells was investigated as a function of cell number under a constant charge/discharge current density (0.1 C/0.1 C). The bipolar 2-/3-stacked cells as well as the mono full cell showed reliable capacity retention with cycling (Fig. 42b, c). All the cells exhibited stable charge/discharge profiles. Most of the (inorganic electrolyte-based) all-solid-state LIBs reported to date were evaluated at high temperatures (above 30 °C) in order to alleviate the problem of slow kinetics observed for the inorganic electrolytes.[35, 36] By contrast, this study exhibited the satisfactory level of electrochemical results at room temperature (*i.e.*, 25 °C), demonstrating the performance viability of the printed bipolar cells.

The charge/discharge profiles of the printed bipolar cells were examined in detail using two mono cells connected in-series or in-plane. In the voltage range from 3.0 to 5.4 V, normal charge/discharge behavior and good coulombic efficiency (~98%) were observed for both the in-series and in-plane configurations (Fig. 42d). Moreover, no substantial difference in the charge/discharge profiles was observed between the two configurations, underlining the versatility and effectiveness of the multistage printing process.

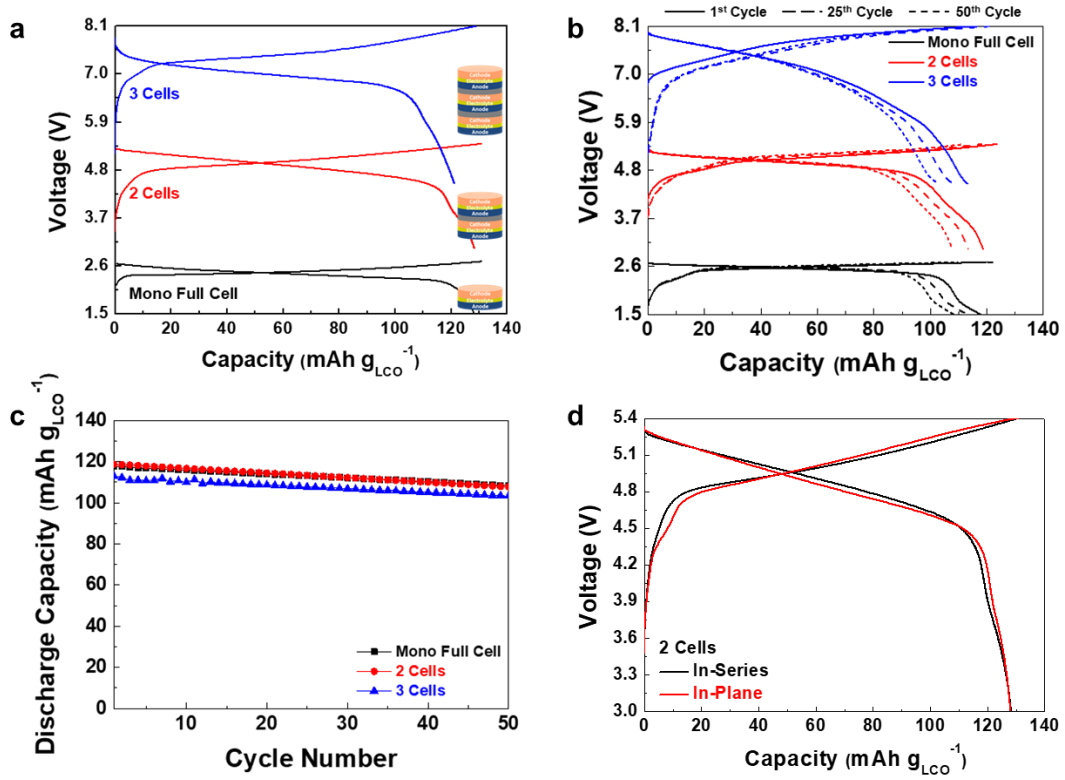

Fig. 41 (a) The charge/discharge profiles of the printed bipolar cells connected in series as a function of cell number (1 - 3 cells). (b) Charge/discharge profiles at 1st, 25th and 50th cycles. (c) Capacity retention as function of cycle number. (d) Comparison of the charge/discharge profiles of the printed bipolar cells (in-series vs. in-plane).

3.2.3.6 Mechanical Flexibility and Thermal Stability of the Printed Bipolar Cells

A critical challenge facing traditional bipolar cells based on inorganic electrolytes is the mechanical stiffness (*i.e.*, poor flexibility). In this study, the printed bipolar 2-stacked cell (here, the two cells were connected in series) with a charge voltage of 5.4 V was subjected to a longitudinal compression cycle (bending radius = 10 mm, deformation rate = 10 mm min^{-1}). No appreciable change in the charge/discharge behavior was observed before/after 100 bending cycles (Fig. 43a). This result shows that the printed GCEs and electrodes, both of which contained flexible semi-IPN skeletons, resulted in dramatic improvement in the mechanical flexibility of the resulting bipolar cells.

In addition to this mechanical flexibility, another advantage of the printed bipolar cells is their safety under harsh operating conditions. The printed bipolar 2-stacked cell continued to power an LED lamp even after being horizontally cut in half (Fig. 43b), exhibiting that both the solid-state GCEs and the gel electrolytes of the printed electrodes were free from leakage problems and prevented electrical contact between the LCO cathode and the LTO anode even after being cut in half. To further demonstrate the solid-state feature of the electrolytes, the printed bipolar 2-stacked cell was exposed to thermal shock (130 °C/0.5 h)[37] conditions. No substantial change in the cell dimensions or in the charge/discharge profiles was observed for the printed bipolar cell. By contrast, a control LCO/LTO cell incorporating the carbonate-based electrolyte (1 M $LiPF_6$ in EC/DMC = 1/1 (v/v)) and a PE separator became severely swollen and eventually lost its electrochemical activity (Fig. 43c).

To highlight the superior safety of the printed bipolar cell, a flammability test was conducted. A bipolar 2-stacked cell was fabricated directly on the curved roof of a miniature toy car using a multi-stage printing process (Fig. 43d). The prepared bipolar cell showed normal charge/discharge profiles (Fig. 43e). After the Al pouch-based packaging substance, which is vulnerable to fire, was removed, the fully charged, printed bipolar 2-stacked cell (in-plane configuration) was exposed to a flame. Notably, the printed cell operated an LED lamp without explosion or structural disruption, whereas the control cell instantly caught fire (Fig. 43f). The remarkable abuse tolerance of the printed cell is attributed to the presence of the nonflammable GCE and electrodes. These safety results demonstrate that the printed bipolar cell is a promising alternative to traditional inorganic-electrolyte-based bipolar cells.

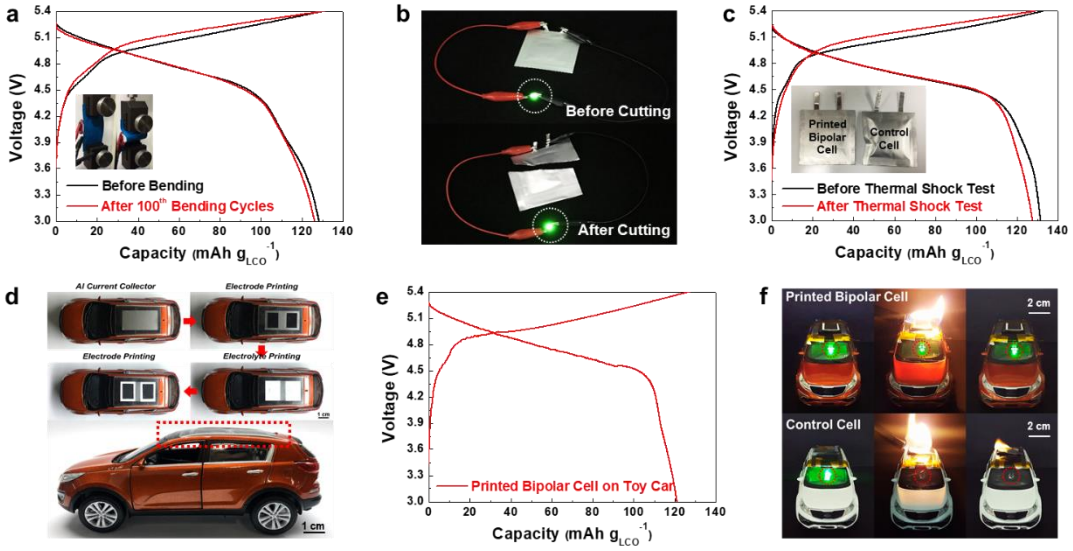

Fig. 42 Mechanical flexibility and thermal stability of the printed bipolar cells. (a) Charge/discharge profiles of the printed bipolar 2-stacked cell (*i.e.*, the two cells were connected in series) before/after 100 bending cycles (bending radius = 20 mm, deformation rate = 200 mm min^{-1}). (b) Photographs showing the safety robustness of the printed bipolar 2-stacked cell. The cell continued to power an LED lamp even after being horizontally cut in half. (c) Charge/discharge profiles of the printed bipolar 2-stacked cell before/after exposure to thermal shock (130 ºC/0.5 h). The photograph of the cell after the thermal shock test, along with that of the control cell (consisting of LCO cathode, LTO anode, carbonate-based electrolyte (1 M $LiPF_6$ in EC/DMC = 1/1 (v/v)) and PE separator) is also shown. (d) Photographs showing the stepwise fabrication of the printed bipolar 2-stacked cell on the curved roof of a miniature toy car. (e) Charge/discharge profiles of the printed bipolar 2-stacked cell on a miniature toy car. (f) Nonflammability test of the printed bipolar 2-stacked cell and control cell; the Al pouch-based packaging substances were removed prior to this test.

3.2.4 Conclusion

In summary, we demonstrated a printed bipolar all-solid-state LIB with exceptional flexibility, shape versatility, charge/discharge behavior, nonflammability and manufacturing simplicity that far exceed those achievable with the currently widespread (sulfide- or oxide-based) inorganic electrolytes. The printed bipolar cells were composed of GCEs (gel electrolytes and Al_2O_3 nanoparticles) and bulk electrodes (LCO or LTO active powder, carbon black additive and gel electrolyte). The gel electrolyte, which consisted of the nonflammable SBN electrolyte and flexible semi-IPN skeleton, was used instead of traditional inorganic electrolytes. The LCO and LTO powders were coated with SWCNTs prior to electrode fabrication to improve their electronic conductivity. The flexible/nonflammable GCEs and electrodes were rheologically tuned and combined with a UV-assisted, stencil-based multistage printing process, eventually enabling facile realization of printed bipolar cells with various form factors (including in-series/in-plane configurations). Notably, the multistage printing did not involve high-pressure/high-temperature sintering processes. Future work will be devoted to replacing the Al_2O_3 nanoparticles with inorganic electrolytes to enhance ionic transport in the printed bipolar cells. The multistage printing-based bipolar cell strategy described herein holds great promise as an effective and scalable platform technology to move bipolar all-solid-state batteries one step closer to commercialization.

3.2.5 References

1. M. Armand; J. -M. Tarascon, Building better batteries, Nature, 2008, 451, 652-657.
2. B. Dunn; H. Kamath; J.-M. Tarascon, Electrical energy storage for the grid: a battery of choices, Science, 2011, 334, 928-935.
3. B. Scrosati; J. Hassoun; Y.-K. Sun, Lithium-ion batteries. A look into the future, Energy Environ. Sci., 2011, 4, 3287-3295.
4. K. Yoshima; Y. Harada; N. Takami, Thin hybrid electrolyte based on garnet-type lithium-ion conductor $Li_7La_3Zr_2O_{12}$ for 12 V-class bipolar batteries, J. Power Sources, 2016, 302, 283-290.
5. Y.-S. Hu; Batteries: getting solid, Nat. Energy, 2016, 1, 16042-16043.
6. Y. Kato; S. Hori; T. Saito; K. Suzuki; M. Hirayama; A. Mitsui; M. Yonemura; H. Iba; R. Kanno, High-power all-solid-state batteries using sulfide superionic conductors, Nat. Energy, 2016, 1, 16030-16036.
7. T. Sato; T. Morinaga; S. Marukane; T. Narutomi; T. Igarashi; Y. Kawano; K. Ohno; T. Fukuda; Y. Tsujii, Novel solid-state polymer electrolyte of colloidal crystal decorated with ionic-liquid polymer brush, Adv. Mater., 2011, 23, 4868-4872.
8. Y. Gambe; Y. Sun; I. Honma, Development of bipolar all-solid-state lithium battery based on quasi-solid-state electrolyte containing tetraglyme-LiTFSA equimolar complex, Sci. Rep., 2015, 5, 8869-8873.
9. T. Matsuo; Y. Gambe; Y. Sun; I. Honma, Bipolar stacked quasi-all-solid-state lithium secondary batteries with output cell potentials of over 6 V, Sci. Rep., 2014, 4, 6084-6088.
10. J. Janek; W. G. Zeier, A solid future for battery development, Nat. Energy, 2016, 1, 16141-16144.
11. Y. J. Nam; S.-J. Cho; D. Y. Oh; J.-M. Lim; S. Y. Kim; J. H. Song; Y.-G. Lee; S.-Y. Lee; Y. S. Jung, Bendable and thin sulfide solid electrolyte film: a new electrolyte opportunity for free-standing and stackable high-energy all-solid-state lithium-ion batteries, Nano Lett., 2015, 15, 3317-3323.
12. N. Kamaya; K. Homma; Y. Yamakawa; M. Hirayama; R. Kanno; M. Yonemura; T. Kamiyama; Y. Kato; S. Hama; K. Kawamoto, A lithium superionic conductor, Nat. Mater., 2011, 10, 682-686.
13. J. van den Broek; S. Afyon; J. L. Rupp, Interface-engineered all-solid-state Li-ion batteries based on garnet-type fast Li^+ conductors, Adv. Energy Mater., 2016, 6, 1600736.
14. H. Wakayama; H. Yonekura; Y. Kawai, Three-dimensional bicontinuous nanocomposite from a self-assembled block copolymer for a high-capacity all-solid-state lithium battery cathode, Chem. Mater., 2016, 28, 4453-4459.
15. W. Liu; N. Liu; J. Sun; P.-C. Hsu; Y. Li; H.-W. Lee; Y. Cui, Ionic conductivity

enhancement of polymer electrolytes with ceramic nanowire fillers, Nano Lett., 2015, 15, 2740-2745.

16. E. Peled; D. Golodnitsky; G. Ardel; J. Lang; Y. Lavi, Development and characterization of bipolar lithium composite polymer electrolyte (CPE)-FeS_2 battery for applications in electric vehicles, J. Power Sources, 1995, 54, 496-500.
17. K. K. Fu; Y. Gong; J. Dai; A. Gong; X. Han; Y. Yao; C. Wang; Y. Wang; Y. Chen; C. Yan, Flexible, solid-state, ion-conducting membrane with 3D garnet nanofiber networks for lithium batteries, P. Natl. Acad. Sci., 2016, 113, 7094-7099.
18. S. -H. Kim; K. -H. Choi; S. -J. Cho; S. Choi; S. Park; S. -Y. Lee, Printable solid-state lithium-ion batteries: a new route toward shape-conformable power sources with aesthetic versatility for flexible electronics, Nano Lett., 2015, 15, 5168-5177.
19. E. -H. Kil; K. -H. Choi; H. -J. Ha; S. Xu; J. A. Rogers; M. R. Kim; Y. G. Lee; K. M. Kim; K. Y. Cho; S. -Y. Lee, Imprintable, bendable, and shape-conformable polymer electrolytes for versatile-shaped lithium-ion batteries, Adv. Mater., 2013, 25, 1395-1400.
20. Q. Wang; P. Pechy; S. M. Zakeeruddin; I. Exnar; M. Grätzel, Novel electrolytes for $Li_4Ti_5O_{12}$-based high power lithium ion batteries with nitrile solvents, J. Power Sources, 2005, 146, 813-816.
21. K. Xu, Electrolytes and interphases in Li-ion batteries and beyond, Chem. Rev., 2014, 114, 11503-11618.
22. D. Zhou; Y.-B. He; R. Liu; M. Liu; H. Du; B. Li; Q. Cai; Q.-H. Yang; F. Kang, In situ synthesis of a hierarchical all-solid-state electrolyte based on nitrile materials for high-performance lithium-ion batteries, Adv. Energy Mater., 2015, 5, 1500353.
23. H.-J. Ha; Y. H. Kwon; J. Y. Kim; S.-Y. Lee, A self-standing, UV-cured polymer networks-reinforced plastic crystal composite electrolyte for a lithium-ion battery, Electrochim. Acta, 2011, 57, 40-45.
24. H.-J. Ha; E.-H. Kil; Y. H. Kwon; J. Y. Kim; C. K. Lee; S.-Y. Lee, UV-curable semi-interpenetrating polymer network-integrated, highly bendable plastic crystal composite electrolytes for shape-conformable all-solid-state lithium ion batteries, Energy Environ. Sci., 2012, 5, 6491-6499.
25. B. R. Shin; Y. S. Jung, All-solid-state rechargeable lithium batteries using $LiTi_2(PS_4)_3$ cathode with Li_2S-P_2S_5 solid electrolyte, J.Electrochem. Soc., 2014, 161, A154-A159.
26. Y. Li; W. Zhou; X. Chen; X. Lü; Z. Cui; S. Xin; L. Xue; Q. Jia; J. B. Goodenough, Mastering the interface for advanced all-solid-state lithium rechargeable batteries, P. Natl. Acad. Sci., 2016, 113, 13313-13317.
27. M. Sano; A. Kamino; J. Okamura; S. Shinkai, Noncovalent self-assembly of carbon nanotubes for construction of “cages”, Nano Lett., 2002, 2, 531-533.

28. E. Menna; F. Della Negra; M. Prato; N. Tagmatarchis; A. Ciogli; F. Gasparrini; D. Misiti; C. Villani, Carbon nanotubes on HPLC silica microspheres, Carbon, 2006, 44, 1609-1613.
29. T. Fujigaya; J. Yoo; N. Nakashima, A method for the coating of silica spheres with an ultrathin layer of pristine single-walled carbon nanotubes, Carbon, 2011, 49, 468-476.
30. J.-M. Kim; J.-H. Park; C. K. Lee; S.-Y. Lee, Multifunctional semi-interpenetrating polymer network-nanoencapsulated cathode materials for high-performance lithium-ion batteries, Sci. Rep., 2014, 4, 4602-4608.
31. J.-H. Park; J.-M. Kim; C. K. Lee; S.-Y. Lee, Mixed ion/electron-conductive protective soft nanomatter-based conformal surface modification of lithium-ion battery cathode materials, J. Power Sources, 2014, 263, 209-216.
32. K.-H. Choi; J. Yoo; C. K. Lee; S.-Y. Lee, All-inkjet-printed, solid-state flexible supercapacitors on paper, Energy Environ. Sci., 2016, 9, 2812-2821.
33. F. Pignon; A. Magnin; J.-M. Piau, Thixotropic behavior of clay dispersions: combinations of scattering and rheometric techniques, J. Rheol., 1998, 42, 1349-1373.
34. S. R. Raghavan; M. W. Riley; P. S. Fedkiw; S. A. Khan, Composite polymer electrolytes based on poly (ethylene glycol) and hydrophobic fumed silica: dynamic rheology and microstructure, Chem. Mater., 1998, 10, 244-251.
35. Y. Zhao; C. Wu; G. Peng; X. Chen; X. Yao; Y. Bai; F. Wu; S. Chen; X. Xu, A new solid polymer electrolyte incorporating $Li_{10}GeP_2S_{12}$ into a polyethylene oxide matrix for all-solid-state lithium batteries, J. Power Sources, 2016, 301, 47-53.
36. Y. Li; W. Zhou; S. Xin; S. Li; J. Zhu; X. Lü; Z. Cui; Q. Jia; J. Zhou; Y. Zhao, Fluorine-doped antiperovskite electrolyte for all-solid-state lithium-ion batteries, Angew. Chem., Int. Ed., 2016, 55, 9965-9968.
37. S.-H. Kim; K.-H. Choi; S.-J. Cho; J.-S. Park; K. Y. Cho; C. K. Lee; S. B. Lee; J. K. Shim; S.-Y. Lee, A shape-deformable and thermally stable solid-state electrolyte based on a plastic crystal composite polymer electrolyte for flexible/safer lithium-ion batteries, J. Mater. Chem. A, 2014, 2, 10854-10861.

List of Publications

(First-author)

1. S. –H. Kim, K. –H. Choi, S. –J. Cho, J. T. Yoo, S. –S. Lee, S. –Y. Lee*, Flexible/Shape-Versatile, Bipolar All-Solid-State Lithium-Ion Batteries Prepared by Multistage Printing, Energy Environ. Sci., 2018, 11, 321.
2. S. –H. Kim, K. –H. Choi, S. –J. Cho, S. Park, S. –Y. Lee*, Printable Solid-State Lithium-on Batteries: A New Route toward Shape-Conformable Power Sources with Aesthetic Versatility for Flexible Electronics, Nano Lett., 2015, 15, 5168.
3. S. –H. Kim, K. –H. Choi, S. –J. Cho, J. –S. Park, K. Y. Cho, C. K. Lee, S. –Y. Lee*, A Shape-Deformable and Thermally Stable Solid-State Electrolyte Based on a Plastic Crystal Composite Polymer Electrolyte for Flexible/Safer Lithium-Ion Batteries, J. Mater. Chem. A, 2014, 2, 10699.
4. S. –H. Kim, K. –H. Choi, S. –J. Cho, E. –H. Kil, S. –Y. Lee*, Mechanically compliant and lithium dendrite growth-suppressing composite polymer electrolytes for flexible lithium-ion batteries, J. Mater. Chem. A, 2013, 1, 4949.

(Co-author)

1. J. Y. Kim, D. O. Shin, S. -H. Kim, J. H. Lee, K. M. Kim, J. Oh, M. J. Lee, Y. -S. Yang, S. -Y. Lee, J. Y. Kim, Y. -G. Lee*, Reversiable thixotropic gel electrolytes for safer and shape-versatile lithium-ion batteires, J. Power Sources, 2018, 401, 126.
2. S. –S. Lee, K. –H. Choi, S. –H. Kim, S. –Y. Lee*, Wearable Supercapacitors Printed on Garments, Adv. Funct. Mater., 2018, 28, 1705571.
3. H. Um, K. –H. Choi, I. Hwang, S. –H. Kim, K. Seo*, S. –Y. Lee*, Monolithically Integrated, Photo-Rechargeable Portable Power Sources Based on Miniaturized Si Solar Cells and Printed Solid-State Lithium-Ion Batteries, Energy Environ. Sci., 2017, 10, 931.
4. K. –H. Choi, S. –J. Cho, S. –H. Kim, Y. H. Kwon, J. Y. Kim, S. –Y. Lee*, Thin, Deformable, and Safety-Reinforced Plastic Crystal Polymer Electrolytes for High-Performance Flexible Lithium-Ion Batteries, Adv. Funct. Mater., 2014, 24, 44.
5. K. –H. Choi, S. –H. Kim, H. –J. Ha, E. –H. Kil, C. K. Lee, S. –Y. Lee*, Compliant polymer network-mediated fabrication of a bendable plastic crystal polymer electrolyte for flexible lithium-ion batteries, J. Mater. Chem. A, 2013, 1, 5224.